Nanoscale

COMMUNICATION

View Article Online
View Journal



Cite this: DOI: 10.1039/d4nr03484h

Received 25th August 2024,
Accepted 22nd October 2024
DOI: 10.1039/d4nr03484h

rsc.li/nanoscale

# Asymmetric [$Dy_2$] molecules deposited into micro-SQUID susceptometers: *in situ* characterization of their magnetic integrity†

Ana Repollés,‡[a] María Carmen Pallarés,‡[a,b] David Aguilà,[c,d] Olivier Roubeau,[a] Verónica Velasco,[c,d] Diego Gella,[a] Leoní A. Barrios,[c,d] María José Martínez-Pérez,[a] Javier Sesé,[a] Dietmar Drung,[e] Jesús Ignacio Martínez,[a] Thomas Schurig,[e] Boris Le Guennic,[f] Anabel Lostao,[a,b,g] Guillem Aromí *[c,d] and Fernando Luis *[a]

**The controlled integration of magnetic molecules into superconducting circuits is key to developing hybrid quantum devices. Herein, we study [$Dy_2$] molecular dimers deposited into micro-SQUID susceptometers. The results of magnetic, heat capacity and magnetic resonance experiments, backed by theoretical calculations, show that each [$Dy_2$] dimer fulfills the main requisites to encode a two-spin quantum processor. Arrays of between $2 \times 10^8$ and $7 \times 10^9$ [$Dy_2$] molecules were optimally integrated under ambient conditions inside the 20 μm wide loops of micro-SQUID sensors by means of dip-pen nanolithography. Equilibrium magnetic susceptibility and phonon-assisted spin tunneling dynamics measured *in situ* substantiate that these molecules preserve spin ground states, magnetic interactions and magnetic asymmetry that characterize them in bulk. These results show that it is possible to interface multi-qubit molecular complexes with on-chip superconducting circuits without disturbing their relevant properties and suggest the potential of soft nanolithography techniques to achieve this goal.**



## Introduction

Molecular nanomagnets are considered good candidates for serving as basic units of future quantum devices.[1] The ability to tune their properties by exploiting chemical synthesis has led to major improvements in spin coherence times, even at relatively high temperatures,[2–5] that put them on a par with other spin and charge solid-state qubits. Chemical design can also be exploited to scale up quantum resources.[6] Molecular and supramolecular structures that encode multiple qubits or, in general, *d*-dimensional qudits in their electronic[7–9] or nuclear[10] spin states, or in a combination of both,[11] have been reported. Embedding nontrivial quantum operations in each repetitive unit, in this case, a molecule, is seen as one of the main competitive advantages of this approach over other quantum computing platforms as it simplifies the implementation of certain algorithms, in particular quantum error correction.[12,13]

However, achieving full scalability remains challenging because it necessarily involves the ability to control and connect many individual molecules.

A promising idea is to bring concepts and technologies developed for superconducting quantum circuits to the realm of molecules.[14–16] The operation of such a hybrid platform sets stringent conditions for the accurate positioning of molecules, ideally under ambient conditions, in suitable locations of a superconducting device.[17,18] A second necessary requisite is that relevant molecular properties be retained under such conditions, which might conflict with the need for maximizing their coupling to the circuit.[19] While the main concern in the case of individual qubits is that the spin coherence time remains sufficiently long, in the case of molecular structures, hosting multiple spins, even the mere definition of the qubit states, can be strongly affected by the environment. These states and, especially, the ability to address each of them arise from a subtle combination of suitable individual spin states,

[a]Instituto de Nanociencia y Materiales de Aragón (INMA), CSIC and Universidad de Zaragoza, Plaza San Francisco s/n, 50009 Zaragoza, Spain. E-mail: fluis@unizar.es
[b]Laboratorio de Microscopias Avanzadas (LMA), Universidad de Zaragoza, 50018 Zaragoza, Spain
[c]Departament de Química Inorgànica i Orgànica, Universitat de Barcelona, Diagonal 645, 08028 Barcelona, Spain. E-mail: aromi@ub.edu
[d]Institut of Nanoscience and Nanotechnology of the University of Barcelona (IN2UB), Barcelona, Spain
[e]Physikalisch-Technische Bundesanstalt (PTB), Abbestraße 2-12, D-10587 Berlin, Germany
[f]Univ Rennes, CNRS, ISCR (Institut des Sciences Chimiques de Rennes) - UMR 6226, F-35000 Rennes, France
[g]Fundación ARAID, 50018 Zaragoza, Spain

†Electronic supplementary information (ESI) available. CCDC 2310387 and 2310388. For ESI and crystallographic data in CIF or other electronic format see DOI: https://doi.org/10.1039/d4nr03484h

‡These two authors contributed equally to this work.

magnetic asymmetry and intramolecular spin–spin couplings, which critically depend on the composition of the molecular core and molecular structure.[7–9] Both aspects can be affected by the loss of crystalline order and interactions with the chip surface that accompany the integration into realistic devices. It is this fundamental aspect that we address in our work.

To this end, we explore molecular complexes hosting two non-equivalent lanthanide ions. The synthesis exploits a protocol that enables selectively obtaining pure homo-[7a,c,20,21] or heterometallic[7b,22,23] species with chemical formula (Hpy)[LnLn′(HL)$_3$(X)(py)$_n$(H$_2$O)$_m$] (py = pyridine, H$_3$L = 6-(3-oxo-3-(2-hydroxyphenyl)propenol)-pyridine-2-carboxylic acid, X = Cl$^-$ or NO$_3^-$, $n + m = 2$), termed here **[LnLn′]** or **[Ln$_2$]**. By direct deposition with dip-pen nanolithography, based on AFM, arrays of **[Dy$_2$]** lanthanide dimers were patterned onto selected areas of suitably designed micro-SQUID superconducting sensors.[24,25] The superconducting device allows characterizing *in situ* their linear magnetic response down to very low temperatures. The ac susceptibility provides information not only on the magnetic moments of the lanthanide ions present in each molecule but also on their mutual interactions and dynamics. The comparison with data measured on the bulk material allows us to critically ascertain whether these molecules retain the ability to encode two addressable spin qubits.

## Results and discussion

In previous reports, we have shown that the different coordination environments of the two metal ions in (Hpy)[Tb$_2$(HL)$_3$(Cl)(py)$_2$] and (Hpy)[Gd$_2$(HL)$_3$(NO$_3$)(py)(H$_2$O)], combined with their mutual weak interaction are critical in turning these molecular systems into appropriate prototypes for two- and six-qubit quantum processors, respectively.[1c,7a,c] In order to probe such properties in a related two-spin system upon deposition onto a superconducting circuit, we synthesized a **[Dy$_2$]** analogue. On account of the large $J = 15/2$ angular momentum of free Dy(III), this complex is expected to display a stronger magnetic response, convenient for the detection of signals from thin layers. The compound crystallizes from pyridine/Et$_2$O following the reaction between DyCl$_3$ and H$_3$L. The structure of **[Dy$_2$]**, shown in Fig. 1 and Fig. S1 of the ESI,† exhibits two Dy(III) ions bridged and chelated by three μ:η$^4$−(HL)$^{2-}$ ligands, each *via* one tri- and one didentate pocket and disposed in a head-to-head-to-tail fashion. The nine-coordination is completed by two py ligands on one metal and by one Cl$^-$ donor on the other. This complex forms an H-bond *via* two COO$^-$ moieties with an Hpy$^+$ cation, thus compensating its negative charge. For comparison purposes, a related **[LaDy]** compound was obtained with the same procedure, using equimolar amounts of Dy(NO$_3$)$_3$ and La(NO$_3$)$_3$ for the reaction. The different coordination sites in the complex allow to selectively discriminate the position of each metal within the molecule selectively based on the ionic radii.[7b,21] The structure of **[LaDy]** (Fig. S2†) is analogous to that of **[Dy$_2$]** with one Dy(III) substituted by La(III), now coordinated by didentate NO$_3^-$ (instead of Cl$^-$) and exhibiting coordination number (CN) of 10. The terminal ligands of Dy(III) are here one py and one H$_2$O. The stability of both compounds in solution as well as the heterometallic nature of **[LaDy]** were shown through mass spectrometry (Fig. S3†).

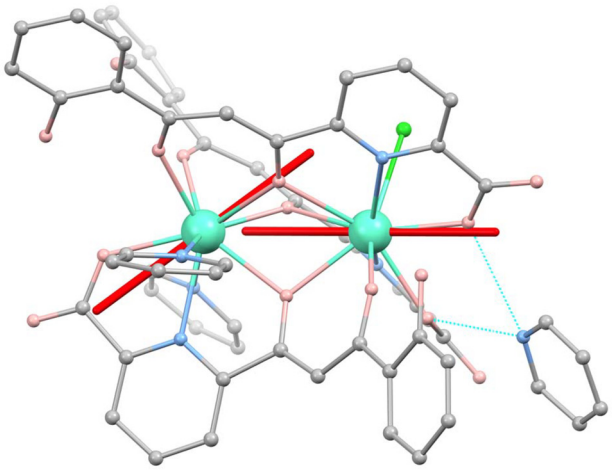

**Fig. 1** Molecular structure of **[Dy$_2$]**. Turquoise is Dy, grey is C, salmon is O, blue is N and green is Cl. Hydrogen atoms are omitted. Hydrogen bonds between Hpy$^+$ and the complex are in dashed blue lines. Orientations of the magnetic easy axes $\vec{z_1}$ and $\vec{z_2}$ of the two Dy(III) ions, determined *via ab initio* calculations (see text and ESI†), are shown as red sticks.

We have tested that **[Dy$_2$]** fulfils the conditions to encode two addressable spin qubits *via* a combination of magnetic susceptibility, heat capacity and electron paramagnetic resonance (EPR) experiments on bulk samples, whose results are shown in Fig. 2a, b and c, respectively.

The molar magnetic susceptibility $\chi$ measured at sufficiently low frequency (1.7 Hz in Fig. 2a) shows the characteristic equilibrium paramagnetic behavior from room temperature down to very low temperatures ($T > 0.15$ K in Fig. 2a). The $\chi T$ product provides direct information on the effective magnetic moments $\mu_{\mathrm{eff}}$ of the two Dy ions and their interactions through the Curie–Weiss law

$$\chi T \simeq 2N_A\mu_{\mathrm{eff}}^2[T/3k_B(T-\theta)] \quad (1)$$

where $\theta$ parameterizes the effect of spin–spin couplings. The decrease in $\chi T$ observed from room temperature down to about 10 K signals the thermal depopulation of excited level doublets, split by the local crystal field acting on each of the two ions. Already at liquid Helium temperatures, only the ground state doublet remains populated and each Dy(III) therefore behaves as an effective spin-1/2 system. The plateau observed in this temperature region is compatible with $\mu_{\mathrm{eff}}^2 = g_{\mathrm{eff}}^2 S(S+1)\mu_B^2$, where $S = \frac{1}{2}$, $g_{\mathrm{eff}} = [(g_x{}^2 + g_y{}^2 + g_z{}^2)/3]^{1/2} \simeq 11.2$, and the $g'_i$s are the principal values of the $\hat{g}$ tensor. These results agree well with the predictions of *ab initio* simulations described in the methods and the ESI,† which point to a strong uniaxial character of both Dy(III) spins. This leads to a ground state doublet whose states are close to the $M_J = \pm 15/2$ angular

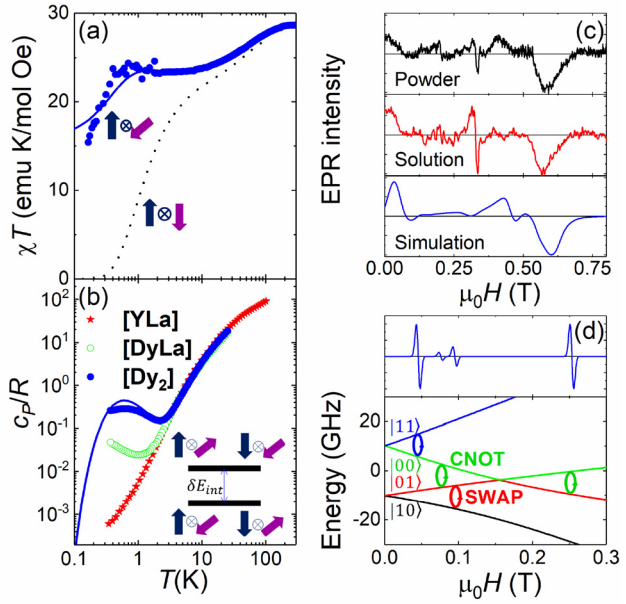


**Fig. 2** Characterization of **[Dy$_2$]** as a two-qubit system. (a) Plot of $\chi T$ *vs.* $T$ between 300 and 0.15 K (dots). The dotted (solid) lines are theoretical predictions for collinear (tilted) magnetic easy axes. They were calculated with $\chi T \simeq \chi_{S=1/2}T[C_0 + C_1(2k_BT/\Delta)\tanh(\Delta/2k_BT) + C_2\tanh(\Delta/2k_BT)]$.[7b,26] Here, $\chi_{S=1/2}$ is the low temperature susceptibility limit, based on the effective spin Hamiltonian (2), $\Delta/k_B$ = 1.3(2) × 10$^2$ K is the energy gap between the first excited and ground elctronic doublets of each Dy ion, and $C_0$, $C_1$ and $C_2$ are fitting coefficients that depend on the wave functions describing these two doublets. The coupling constant $J_{12}/k_B$ was fixed to −0.023 K (−0.014 K) for tilted (collinear) axes, which accounts for the low-$T$ specific heat data. (b) Molar specific heat of **[Dy$_2$]**, **[LaDy]** and **[LaY]** at zero magnetic field. The solid line is a calculation that includes the magnetic contribution derived from eqn (2) plus the lattice contribution obtained from the **[LaY]** data. (c) Continuous wave X-band EPR spectra of **[Dy$_2$]** at 6 K in bulk powder form (top) and in solution (middle). The bottom panel shows a simulation based on eqn (2) with the same parameters used to calculate the magnetic susceptibility and the specific heat. (d) Bottom: scheme of the 4 lowest lying spin levels of a **[Dy$_2$]** molecule, calculated with eqn (2) for a magnetic field forming 55 degrees with $\overrightarrow{z_1}$. The magnetic asymmetry and spin–spin coupling lead to unequally spaced levels. Different transitions, shown in the EPR simulation (top), can then be addressed by microwave resonant pulses. This allows encoding two addressable spin qubits and performing conditional quantum operations.

momentum projections, well separated energetically from all excited doublets.

The second drop in $\chi T$ observed below 1 K indicates a weak antiferromagnetic coupling between the two Dy ions. This interaction splits the energies of different mutual spin orientations. The splitting $\delta E_{int}$ can be detected, even at zero magnetic fields, by means of heat capacity experiments. Fig. 2b and S9† compare the molar specific heat $c_P$ of **[Dy$_2$]** with that measured on the **[LaDy]** "monomer". At low temperatures, where the contributions of magnetic excitations overcome those associated with molecular vibrations (estimated from the results obtained for the diamagnetic complex **[LaY]**),[7b] $c_P$ of **[Dy$_2$]** shows a Schottky-like anomaly that is clearly absent for **[LaDy]**. It is then natural to associate this contribution with the energy splitting between the antiparallel and parallel spin orientations in **[Dy$_2$]**. The temperature of the specific heat maximum $T_{max}$ allows estimating $\delta E_{int} \simeq k_B T_{max}/0.42$ = 1.50(5) K.

On the basis of the above considerations, it follows that the low-$T$ magnetic behavior of **[Dy$_2$]** can be understood within a model of two weakly coupled effective $S = \frac{1}{2}$ spins, described by the following spin Hamiltonian[7b]

$$\mathcal{H} = -\mu_B \vec{H}\hat{g_1}\overrightarrow{S_1} - \mu_B \vec{H}\hat{g_2}\overrightarrow{S_2} - \frac{J_{12}}{g_J{}^2}\overrightarrow{S_1}\hat{g_1}\hat{g_2}\overrightarrow{S_2} \qquad (2)$$

that includes the Zeeman interaction terms of the spins $\overrightarrow{S_1}$ and $\overrightarrow{S_2}$ with the magnetic field $\vec{H}$ and a spin–spin coupling, where $J_{12}$ is the coupling constant and $g_J$ = 4/3 is the Landé factor of free Dy(III). It is possible to use eqn (2) to simulate both $\chi T$ and $c_P/R$. The results, shown in Fig. 2a and b, reveal the need to introduce an asymmetry between the Zeeman interactions of the two ions. As Fig. 2a shows, if the principal values and the axes of $\hat{g_1}$ and $\hat{g_2}$ were the same, the cancellation of the two magnetic moments in the ground state would lead to a rapid decrease of $\chi T$ towards zero (dotted line in Fig. 2a) that is not observed experimentally.

For simplicity, we have accounted for the asymmetry by introducing a tilt between the easy magnetization axes of the two ions, which we take along the $\overrightarrow{z_1}$ and $\overrightarrow{z_2}$ principal axes (see Fig. 1). The experimental $\chi T$ and $c_P/R$ data are compatible with a rotation of $\overrightarrow{z_2}$ (and $\overrightarrow{y_2}$) around $\overrightarrow{x_1} = \overrightarrow{x_2}$ by $\delta$ = 52 degrees. Besides, they suggest that $g_x$ and $g_y \ll g_z$, thus in the calculations shown in Fig. 2a and b, we have made both of them equal to zero and set $g_{1z} = g_{2z}$ = 19.1, in order to reduce the number of parameters. These assumptions are supported by the *ab initio* calculations, which give $g_z$ = 18.2–19.5 and $g_{x,y}/g_z \lesssim 0.01$ for both Dy(III) ions (see Tables S5 and S6†). Besides, they predict that $\overrightarrow{z_1}$ and $\overrightarrow{z_2}$ are tilted by about 72 degrees, in fair agreement with the estimate obtained from $c_P/R$ and $\chi T$ (Fig. 1 and S12†).

In spite of its simplifications, the two-spin model (eqn (2)) has the advantage of accounting well for the main features of the magnetic susceptibility and specific heat results. It also accounts for the low-$T$ EPR spectra, shown in Fig. 2c, with the same parameters, provided that $g_x$ and $g_y$ are non-strictly zero but still $g_{x,y}/g_y \lesssim 0.01$. Besides, it grasps the essential aspects that determine the potential of **[Dy$_2$]** to encode two spin qubits. In particular, any magnetic field makes the two Dy ions within **[Dy$_2$]** magnetically inequivalent (*i.e.* it induces a different Zeeman splitting on each of them). The 4 lowest lying spin energy levels of **[Dy$_2$]** become then unequally spaced at any magnetic field $H > 0$. This level of anharmonicity, which ensues from the combination of distinct local coordination sites and a weak spin–spin coupling, constitutes the key ingredient that allows spectroscopically addressing each resonant spin transition. For instance, Fig. 2d shows how a CNOT conditional gate can be implemented *via* the application of a single resonant pulse. The nonzero, albeit small, transverse $g_x$ and $g_y$ factors (Tables S4 and S5†), combined with the off-diag-

onal spin–spin interaction terms and with the non-collinear axes guarantee that these operations are not forbidden,[27] which is indeed confirmed by the EPR results and simulations shown in Fig. 2 and S11.†

In what follows, we consider to what extent these properties are preserved when the molecules are integrated from solution into a superconducting device. The device was a micro-SQUID ac susceptometer, shown in Fig. 3a, specifically designed to achieve the sensitivity needed to detect the minute linear response of a few molecular layers.[25] Arrays of [$Dy_2$] molecular deposits were patterned, under ambient conditions and without any intermediate functionalization, by traversing the AFM tip of a Dip Pen Nanolithography (DPN) system,[18,24b,25,28,29] coated with the molecular "ink", over the surface and contacting it in the form of a predefined pattern, as shown in Fig. 3b. The stability of [$Dy_2$] in the solution was tested by EPR (Fig. 2c) and by UV-Vis spectrophotometry (Fig. S4†). The spatial resolution of AFM allows generating patterns that match the 20 μm wide micro-SQUID pick-up coils (see Fig. S5 and S6†). This allows optimizing the flux coupling between the sample and the micro-SQUID, thus the sensitivity to the magnetic response of the molecules.

Once dried under vacuum, the deposits were analyzed by optical and AFM imaging. In order to accurately determine the amount of [$Dy_2$] transferred into the chip, control deposits of the solvent and glycerol that form part of the ink were also prepared under the same conditions (Fig. S5†). Topographic images and profiles of one of the arrays are shown in Fig. 3c and d, respectively. Repeating successive tip coating and deposition steps gives rise to arrays with an increasing number of molecular dots and with larger thicknesses. Three of them, with 3, 8 and 34 molecular layers, were characterized magnetically down to very low temperatures. We refer to them as $[Dy_2]_{DPN1}$, $[Dy_2]_{DPN2}$ and $[Dy_2]_{DPN3}$, respectively (see Fig. S6†).

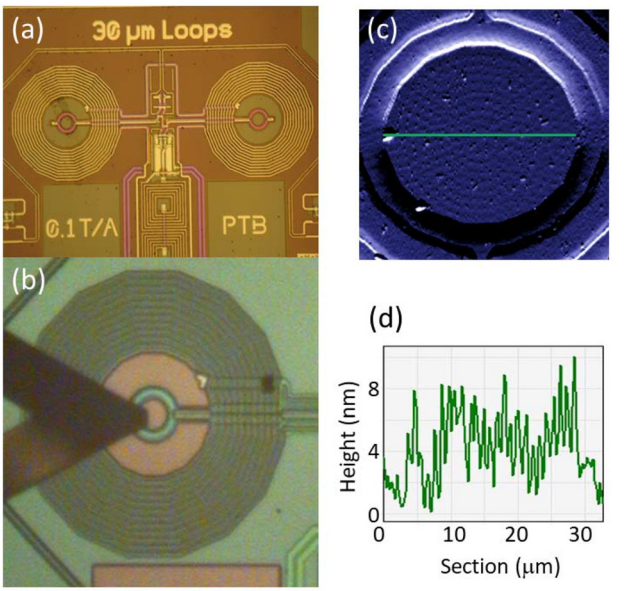


**Fig. 3** Integration of [$Dy_2$] nano-deposits into superconducting devices. (a) Image of a micro-SQUID ac susceptometer. The micro-SQUID is made of two gradiometric loops (coloured in magenta), which act as pick-up coils. They are surrounded by two identical excitation coils that generate the ac magnetic field, perpendicular to the chip's surface. (b) Image of the DPN system AFM tip traversing the area defined by one of the pick-up coils during a deposition process. (c) and (d) Topographic image and height profile measured along the green line of a molecular deposit labelled as $[Dy_2]_{DPN1}$, made of 3 molecular layer thick dots. The number of [$Dy_2$] molecules transferred to the device is $\sim 2 \times 10^8$.

With its gradiometric design (Fig. 3a), the micro-SQUID acts as the pick-up loop of an ac susceptometer. The response of the molecular spins to the ac magnetic field $\overrightarrow{h_{ac}} \cos \omega t$ generated by the excitation coils (Fig. 3b) creates a net flux proportional to $h_{ac}\chi$, which the micro-SQUID converts into a voltage read-out by a lock-in detection system.

Fig. 4 shows results, in terms of net magnetic flux per magnetic field, measured on bulk [$Dy_2$] and on the $[Dy_2]_{DPN3}$, $[Dy_2]_{DPN2}$ and $[Dy_2]_{DPN1}$ deposits. These data show the ability of the device to detect the minute signal generated by the linear magnetic response of the [$Dy_2$] spins. Besides, the susceptibility of the deposits shows qualitatively similar dependences on temperature and frequency as the bulk material. Numerical simulations of the flux coupled to the SQUID were performed by a finite elements method that uses the susceptibility found for the bulk sample, the spatial dependence of $h_{ac}$ and the sample geometry to determine the contribution of each molecular dot. Details are given in the ESI.† They give results, shown in the bottom panels of Fig. 4, quite comparable to those found experimentally, thus suggesting that the spin states are preserved.

Since the magnetic behaviour remains paramagnetic for all samples, we can again use the $\chi T$ product to obtain more precise information on the magnetic moments present in each molecule and on its mutual interactions. As with the bulk sample, we consider first the temperature dependence of the equilibrium susceptibility, obtained at sufficiently low $\omega$ (1.7 Hz) and sufficiently high $T$ ($\gtrsim$0.15 K). The experimental $\chi T$ curves were scaled to molar units using data measured at $T$ = 1 K. They are plotted in Fig. 4i. For all [$Dy_2$] arrays, $\chi T$ shows a drop below 1 K that resembles, within the experimental uncertainties, that found for the bulk material. Besides, it remains, at any temperature, much higher than the prediction (dotted line in Fig. 4i) for perfectly compensated spins. These results show: (1) that the molecular cores transferred to the chips retain two mutually interacting Dy ions and (2) that the two Dy ions remain magnetically inequivalent.

The frequency dependence of the ac susceptibility reveals the existence of spin relaxation processes with time scales $\gtrsim 1/\omega$. Besides, the linear susceptibility acquires an out-of-phase component $\chi''$ that reaches its maximum when the typical spin relaxation time $\tau$ becomes equal to $1/\omega$.[30] Using the data measured at different frequencies, shown in Fig. S10,† we have estimated the temperature dependence of $\tau$ for [LaDy] and for all [$Dy_2$] samples but one, $[Dy_2]_{DPN1}$, whose $\chi''$ signal was below the sensitivity of micro-SQUID. The results are shown in Fig. 5a.

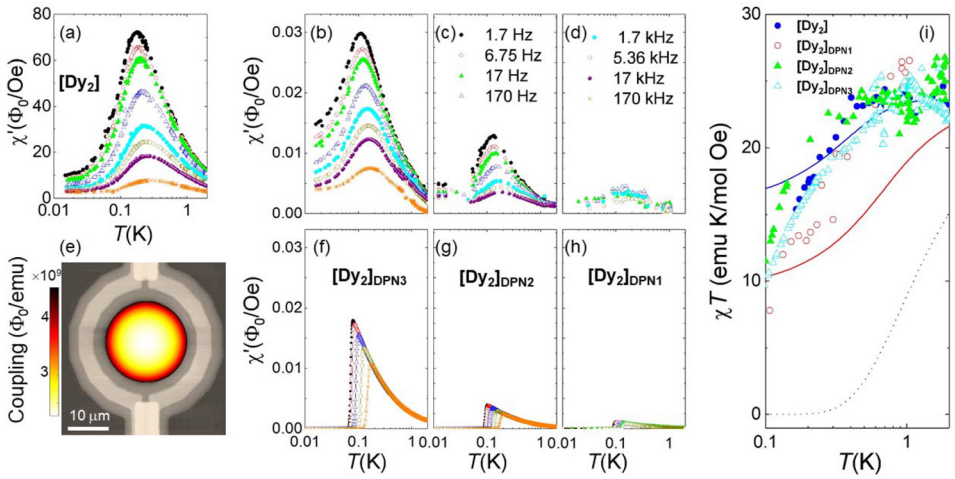


**Fig. 4** *In situ* determination of the magnetic susceptibility of **[Dy$_2$]** deposits. Frequency-dependent flux coupled to the micro-SQUID by the bulk **[Dy$_2$]** sample (a) and **[Dy$_2$]$_{DPN3}$** (b), **[Dy$_2$]$_{DPN2}$** (c) and **[Dy$_2$]$_{DPN1}$** (d) deposits, normalized by the amplitude $h_{ac}$ (= 0.011, 0.5, 0.25 and 0.05 Oe, respectively) of the ac magnetic excitation field at the SQUID centre. (e) Image of the simulated flux sensitivity factor, in units of magnetic flux coupled to the sensor per unit of magnetic moment induced on the sample, calculated for **[Dy$_2$]$_{DPN3}$** and superimposed onto an image of the micro-SQUID loop. These simulations give predictions for the magnetic susceptibility (panels (f–h)), which can be compared to experimental results without any fitting parameters. (i) $\chi T$ products derived from the low-frequency, equilibrium limit of the same data, scaled at $T$ = 1 K. The lines show the predictions that follow from eqn (2) for collinear easy axes (black, dotted line) with $J_{12}/k_B$ = −0.014 K, and for easy axes tilted by either 44 degrees (red, solid line) or 52 degrees (blue, solid line), with $J_{12}/k_B$ = −0.023 K.

The spin relaxation times of **[Dy$_2$]** and of **[LaDy]** follow the Arrhenius law $\tau = \tau_0 \exp(U/k_BT)$ that characterizes a thermally activated process (Fig. 5). The low activation energy values, $U/k_B$ = 2.2(1) K and 0.8(5) K for bulk **[Dy$_2$]** and **[LaDy]**, respectively, show that the relaxation processes involve only states belonging to the ground electronic states of the Dy ions since the excited levels lie more than 100 K above them (Fig. 2a). This result confirms that direct transitions between the 4 lowest-lying electronic spin states are not forbidden, as already shown by EPR data. Besides, the fact that the activation energy of the **[Dy$_2$]** dimer is nearly three times larger than that found for **[LaDy]** suggests that the spin–spin interaction leaves an imprint on the spin dynamics.

The physical nature of the relaxation mechanism can be qualitatively understood by considering how hyperfine and spin–spin couplings hinder the reversal of each Dy spin. The basic ideas are illustrated schematically in Fig. 5b. About 44% of the naturally occurring Dy isotopes ($^{161}$Dy and $^{163}$Dy) carry an $I$ = 5/2 nuclear spin. Their electronic spin ground state doublet is then split by the hyperfine interaction, which can be described by introducing an additional term $\vec{S}\hat{A}\vec{I}$ to the effective spin Hamiltonian (2), where $\hat{A}$ is the effective hyperfine tensor. Because of the strong anisotropy of the electronic spin, this term mainly introduces a zero-field splitting $A_z m_S m_I$. The energy detuning between up and down electronic spin states having the same nuclear spin projection effectively suppresses direct spin tunnelling processes and forces the system to "borrow" energy from lattice vibrations.[31–33] A similar effect is caused by the interactions between electronic spins, either located in different molecules (like in **[LaDy]**) or within each of them (in **[Dy$_2$]**). Irrespective of the specific, and complex, details of the resulting dominant relaxation paths, it then follows that the intra-molecular spin–spin interaction always adds an additional hurdle for the relaxation of the Dy electronic spins (Fig. 5b). The fact that the difference between the activation energies found for **[Dy$_2$]** and **[LaDy]** approximately matches $\delta E_{int}$ provides support for this interpretation.

This also means that the experimental $U$ can be used to characterize spin–spin interactions in **[Dy$_2$]** molecules patterned onto devices. The relaxation times of **[Dy$_2$]$_{DPN2}$** and **[Dy$_2$]$_{DPN3}$**, also shown in Fig. 5, follow Arrhenius laws with activation energies $U/k_B$ = 2.4(2) and 1.6(2) K, respectively, which are significantly larger than the value measured for **[LaDy]**. This confirms that the intramolecular spin–spin coupling is preserved within each of them and, therefore, the composition of the molecular cores remains also intact. Also, they suggest that transitions between different spin states remain as allowed as they are in bulk. Notice that $\tau$ measured at the zero magnetic field is independent of the molecular orientation. Therefore, the differences in $U$ observed between different deposits and with respect to the bulk must arise from modifications in the spin–spin interactions that determine the dominant spin relaxation paths (see Fig. 5). Diverse effects can play roles when molecules are patterned onto a device. On the one hand, the molecular packing differs from that in the crystal, and this directly influences intermolecular dipolar interactions. On the other hand, the same effect combined with the coupling of the bottom molecular layers to the chip substrate, can introduce some strain[25] and thus generate molecular distortions. The experimental $\chi T$ data, shown in Fig. 4i, suggest that such modifications cannot be large. Yet, changes in the mutual orientations of the two Dy(III) easy axes of the order of

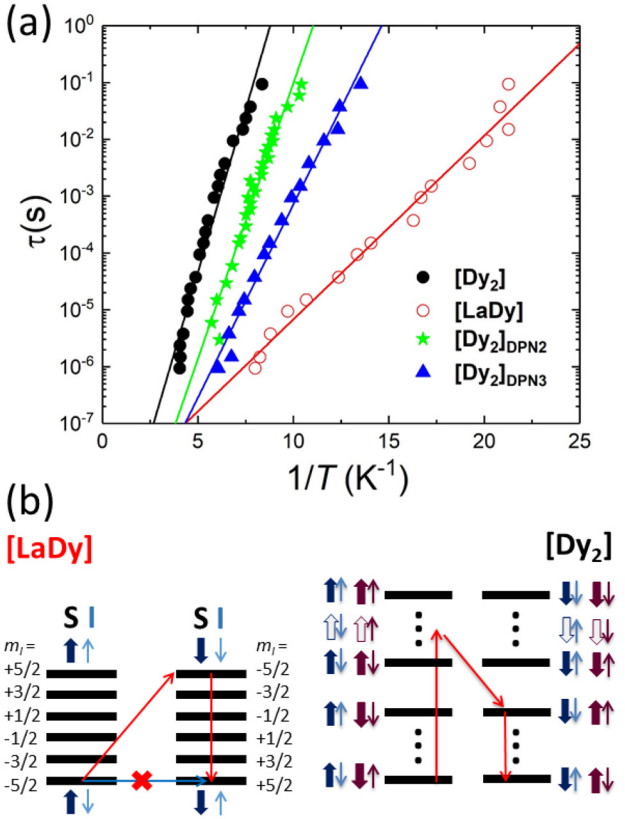


**Fig. 5** Spin relaxation *versus* hyperfine and spin–spin interactions. (a) Arrhenius plot of the spin–lattice relaxation times of bulk **[$Dy_2$]** and **[LaDy]** samples, and of the $[Dy_2]_{DPN2}$ and $[Dy_2]_{DPN3}$ deposits, determined from the imaginary component of the ac magnetic susceptibility measured with a micro-SQUID sensor. Solid lines are least-squares Arrhenius fits, which allow the determination of the dominant activation energies governing the spin reversal. (b) Schematic of possible spin relaxation paths in the presence of hyperfine interactions (left) and spin–spin couplings (right). These interactions block direct spin tunnelling processes and force the spins to relax *via* thermally activated intermediate spin states.

5 degrees could still be compatible with these results, taking into account the experimental uncertainties, and they could affect *U via* the modification of the intra-molecular spin–spin couplings.

## Conclusions

In summary, we have found that **[$Dy_2$]** molecules fulfil all requisites to embody two spin qubits and that they can be delivered with high precision and under ambient conditions into specific areas of a superconducting circuit. Thanks to the high sensitivity of this micro-SQUID device, we have been able to detect *in situ* the linear magnetic response of **[$Dy_2$]** dot arrays consisting of 34, 8 and 3 molecular layers and show that they largely retain their equilibrium and dynamical magnetic behaviour in spite of the lost crystallinity and the increasing effect of the interface with the substrate. In particular, the experiments confirm that the magnetic asymmetry and the spin–spin coupling remain close to those found for the crystalline material.

It is worth emphasizing that chemical design and DPN can be jointly exploited to deliver suitable doses of the functional molecules, *e.g.* by starting from the right solution with a majority of diamagnetic equivalents, such as **[YLa]**. Besides, the spin relaxation time, which ultimately limits the spin coherence for quasi-isolated molecules, is found to reach values as long as 100 ms both in bulk and in the molecular arrays. In conclusion, the results of this work support molecular complexes hosting multiple spin centres as promising building blocks for a hybrid quantum computing architecture and provide useful techniques for testing and realizing it with practical devices.

## Materials and methods

### Materials synthesis

All reactions were performed under aerobic conditions, using the reagents as received. The ligand 6-(3-oxo-3-(2-hydroxyphenyl)propionyl)pyridine-2-carboxylic acid ($H_3L$) was synthesized as previously described.[20]

**Synthesis of (Hpy)[$Dy_2(HL)_3(Cl)(py)_2$] ([$Dy_2$], Fig. S1†).** A yellow solution of $H_3L$ (30.0 mg, 0.11 mmol) in pyridine (10 mL) was added into a pyridine solution (10 mL) of $DyCl_3{\cdot}6H_2O$ (26.4 mg, 0.07 mmol). After stirring for 2 hours, the resulting yellow solution was layered with $Et_2O$. Crystals of **[$Dy_2$]** were recovered after two weeks in 63% yield. IR (KBr pellet, $cm^{-1}$): 3393 mb, 1618 s, 1585 s, 1560 m, 1526 s, 1464 m, 1401 s, 1325 m, 1298 m, 1239 w, 1208 w, 1147 w, 1121 w, 1058 w, 950 w, 891 w, 74 w, 707 w, 665 w, 636 w, 569w. Calculated elemental analysis for **[$Dy_2$]**·1.2py·$4H_2O$ (exp.): C = 47.72 (47.52); H = 3.35 (3.03); N = 5.66 (5.67). MALDI-TOF: $m/z$ = 1176.10 $[Dy_2(HL)_3] + H^+$, (Fig. S3†).

**Synthesis of (Hpy)[$LaDy(HL)_3(NO_3)(py)(H_2O)$] ([LaDy], Fig. S2†).** A yellow solution of $H_3L$ (30.0 mg, 0.11 mmol) in pyridine (10 mL) was added into a colourless pyridine solution (10 mL) of $La(NO_3)_3{\cdot}6H_2O$ (15.2 mg, 0.035 mmol) and $Dy(NO_3)_3{\cdot}6H_2O$ (16.0 mg, 0.035 mmol). After stirring for 1 hour, the resulting slightly turbid yellow solution was filtered and the filtrate was layered with $Et_2O$. Crystals of **[LaDy]** were recovered after two weeks in 67% yield. IR (KBr pellet, $cm^{-1}$): 3414 mb, 1638 m, 1618 s, 1585 w, 1529 m, 1464 m, 1400 s, 1385 s, 1298 m, 1240 w, 1121 w, 1058 m, 949 m, 891 w, 758 w, 705 m, 665 w, 618 w, 568 w. Calculated elemental analysis for **[LaDy]**·$3.6H_2O$ (exp.): C = 45.39 (44.93); H = 3.27 (2.79); N = 5.77 (5.57). ESI MS: $m/z$ = 1152.98 ($[LaDy(HL)_3] + H^+$, Fig. S3†).

### Patterning of [$Dy_2$] deposits *via* Dip-Pen nanolithography

Dip Pen Nanolithography (DPN) was carried out using a high-performance DPN5000 AFM-based system (NanoInk Inc., USA). Silicon nitride triangular DPN single probes (Advanced Creative Solutions Technology, USA) were used for the patterning experiments. The molecular "ink" was prepared by dissol-

ving 30 mg $mL^{-1}$ of **[$Dy_2$]** in a 90/10 v/v DMSO/glycerol mixture. Glycerol was added to increase the viscosity and slow down ink evaporation.[29] The integrity of the molecular complex in solution and their stability over time were checked for different solvents by UV-visible spectrophotometry (Fig. S4†). Prior to the DPN deposition, the sensor was cleaned with ultra-pure ethanol and acetone, and dried by blowing nitrogen gas. The tip coating procedure first involved leaving a drop of the ink into one of the reservoirs of a microfluidic inkwell delivery chip-based system (Advanced Creative Solutions Technology, USA) using a micropipette. Afterwards, the ink was transferred to a microwell through a microchannel, where the DPN tip was dipped and coated with minute amounts of the ink. DPN experiments were carried out under constant conditions at 26 °C and 40% relative humidity using an integrated environmental chamber. The molecular microdeposits were generated by traversing the tip over the surface in the form of the desired pattern, which was previously designed and calibrated using the InkCad software (NanoInk, Inc., USA).

Different patterns were fabricated to check the ability to deposit nanostructures of different forms and layer thicknesses adapted to the inner susceptometer circle, which has an approximate radius of 10 μm (see Fig. 3 and Fig. S5 and S6†). Arrays formed by circular patterns of hundreds to thousands of identical dots were deposited inside the pickup coil and, in parallel, on silicon substrates under the same experimental conditions. The latter facilitates a more precise determination of the pattern's dimensions and thicknesses.

Three samples gave a detectable magnetic response. These were arrays of circular molecular deposits made of approximately 3, 8 and 34 **[$Dy_2$]** molecular layers, which we labelled as $[Dy_2]_{DPN1}$, $[Dy_2]_{DPN2}$ and $[Dy_2]_{DPN3}$, respectively. They are shown in Fig. S6.† The layers were organized by successive coating and deposition steps. The bigger sample was prepared after three successive deposition steps. In $[Dy_2]_{DPN2}$ and $[Dy_2]_{DPN3}$, the circular dots merge to form quasi-continuous films (see Fig. S6†). The solvent and glycerol that form a part of the ink were also deposited under the same conditions as the control. The patterns geometries and topographies were characterized by optical and AFM imaging once dried under a vacuum. The number of molecular layers was estimated using an average diameter of approximately 1.2 nm for each **[$Dy_2$]** molecule, derived from the crystallographic data.

## Physical characterization

**Single crystal X-ray diffraction.** Data for compounds **[$Dy_2$]** and **[LaDy]** were collected at 150 K on a yellow block of dimensions 0.12 × 0.10 × 0.08 $mm^3$ and a yellow lath of dimensions 0.23 × 0.05 × 0.02 $mm^3$, respectively, using an Oxford Diffraction Excalibur diffractometer with enhanced MoKα radiation ($\lambda$ = 0.71073 Å) at the X-ray diffraction and Fluorescence Analysis Service of the SAI-Universidad de Zaragoza. Cell refinement, data reduction, and absorption corrections were performed with the CrysAlisPro suite.[34] The structures were solved by intrinsic phasing with SHELXT[35] and refined by full-matrix least-squares on $F^2$ with SHELXL.[36] The position of the N atom was ascribed on the basis of the residual electron density peaks, before refining with displacement parameters restraints (SIMU and DELU). The difference in electron density is small but real. Upon refinement of these lattice pyridines with their hydrogens placed at calculated positions, any misassignment of C/N atoms typically shows off through too-short contact(s) of the misassigned C–H. This is not the case here. Therefore, while the C/N assignments suffer from some uncertainties, the reported structural models are reasonable. The metal site distribution in **[LaDy]** was confirmed by refining the structure with the two homometallic situations as well as with the inverted Ln sites. These resulted in relatively poorer agreement factors and most importantly in unrealistic combinations of $U_{eq}$ values at the metal sites. In the structure of **[LaDy]** a portion of the lattice pyridine molecules is too diffuse to be modelled, which was analyzed and taken into account with PLATON/SQUEEZE.[37] Crystallographic and refinement parameters are summarized in Table S1.† Selected bond lengths and angles and hydrogen bond details are given in Tables S2 and S3,† respectively.

**Mass spectrometry.** MALDI-TOF mass spectrometry measurements were performed on a 400 ABSciex MALDI-TOF spectrometer at the Unitat d'Espectrometria de Masses de Caracterització Molecular (CCiT) of the University of Barcelona. Crystals of **[$Dy_2$]** were dissolved in mixtures of MeOH with a minimal amount of DMSO. Then, 0.5 μL of an internal reference solution, containing 10 mg $mL^{-1}$ of DCTB in dichloromethane, was added before the injection. Positive-ion ESI mass spectrometry experiments were performed by using an LC/MSD-TOF (Agilent Technologies) with a dual source equipped with a locking spray for internal reference introduction, at the Unitat d'Espectrometria de Masses from the Universitat de Barcelona. Experimental parameters: capillary voltage 4 kV, gas temperature 325 °C, nebulizing gas pressure 103.42 kPa, drying gas flow 7.0 L $min^{-1}$ and fragmentor voltage 175–250 V. Internal reference masses were $m/z$ 121.05087 (purine) or 922.00979 (HP-0921). Crystals of **[LaDy]** were dissolved in mixtures of MeOH with a minimal amount of DMSO and introduced into the source by using an HPLC system (Agilent 110) with a mixture of $H_2O/CH_3CN$ (1 : 1) as the eluent (200 μL $min^{-1}$). As observed previously for related clusters, the ionization caused the removal of terminal nitrate, pyridine and water ligands from the complexes. Moieties related almost exclusively to the expected **[LaDy]** metal composition were observed (see Fig. S3†), with only minimal signals from homometallic moieties detected, thus evidencing not only the realization of the heterometallic compound but also its robustness and exclusiveness in solution.

**Image characterization.** Atomic Force Microscopy (AFM) images were taken using the Tapping Mode with silicon TESPA and nitride SNL cantilevers (Bruker Probes) having 320 kHz and 18–65 kHz nominal resonant frequencies, respectively. Imaging was performed with the AFM of the DPN5000 system and with a MultiMode 8 (Bruker) AFM. The images were analyzed and processed using SPIP (Scanning Probe Image

Processor; Image Metrology) and WSxM software[38] for SPM image processing. Field-Emission Scanning Electron Microscopy (FESEM) images were obtained through the Servicio de Apoyo a la Investigación-SAI, Universidad de Zaragoza, on a Carl Zeiss MERLIN microscope provided with an Energy Dispersive Spectroscopy (EDS) detector INCA 350 from Oxford Instruments. The samples were coated with a few nm of carbon before measurements.

**Heat capacity.** Data were obtained with a commercial physical property measurement system (PPMS, Physical Measurements unit of the Servicio de Apoyo a la Investigación-SAI, Universidad de Zaragoza) that makes use of the relaxation method.[39,40] The samples, in polycrystalline form, were pressed into pellets and placed onto the calorimeter on top of a thin layer of Apiezon N grease that fixes the sample and improves the thermal contact. The raw data were corrected from the known contributions arising from the empty calorimeter and the grease.

**Magnetic measurements.** Variable-temperature (2–300 K, at 0.5 T applied dc field) and variable-field (0–5 T, at 2 and 5 K) magnetization data for the bulk **[Dy$_2$]** and **[LaDy]** polycrystalline solids were obtained with a Quantum Design MPMS-XL through the Servicio de Apoyo a la Investigación-SAI, Universidad de Zaragoza. Corrections for the sample holder contribution and the intrinsic diamagnetism of the sample were applied, as determined empirically and estimated using Pascal constants, respectively.

### Electron paramagnetic resonance experiments

Continuous wave Electron Paramagnetic Resonance (EPR) experiments were performed with a commercial Elexsys E-580 system by Bruker, operating in the X-band. The spectrometer consists of a resonant cavity, in which the paramagnetic sample was placed and located at the centre of a 1.4 T electromagnet. An rf modulation field generated by a set of small coils results in a derivative-like detection of each absorption resonance. A gas-flow Helium cryostat was used to reach and control temperature in the vicinity of 6 K. EPR measurements were performed on the polycrystalline powder (9.483 GHz) and a frozen solution (9.475 GHz) placed in quartz tubes. The solution was obtained by dissolving 2.40 mg of polycrystalline **[Dy$_2$]** in 2 drops of d$^6$-DMSO and a mixture of 500 μL : 500 μL d$^6$-EtOH : d$^4$-MeOH, for a concentration of *ca.* 1.42 mM. No spin-echo could be detected.

Simulations were done with Easyspin[41] and the spin Hamiltonian described in the main text, fixing $g_x = g_y = 0.1$ and $g_z = 19.1$ for both Dy sites, an angle between their $z$-axis of 53° and $J_{12}/k_B = -0.023$ K.

### Very low temperature ac susceptibility measurements

These were performed with integrated micro-SQUID susceptometers developed at the Physikalisch-Technische Bundesanstalt. They are made of Nb deposited on Si/SiO$_2$ wafers and are fabricated by optical lithography. Experiments on bulk **[Dy$_2$]** and **[LaDy]** samples were performed using susceptometers made of ≃800 × 400 μm$^2$ banana-shaped excitation and pick-up coils coupled to a micro-SQUID sensor, as described in ref. 42 and 43. Fig. S7† shows an image of one of these devices. A different circuit design[25,44] was applied to the detection of the minute signals associated with the linear response of the molecular deposits. In this case, the micro-SQUID sensor itself, with a gradiometric design, acts as the pick-up loop of the ac magnetic susceptometer. The coupling between the sample and the sensor is favoured by the reduced diameter (30 μm) of its two circular loops. Two identical ac excitation coils allow the application of ac magnetic fields with amplitudes of up to 3 Oe. The output signal when no sample is present is minimized by the close-to-perfect reflection symmetry of the setup. Its frequency and temperature dependences were characterized on a bare circuit and then subtracted from the experimental results. This instrument exhibits a white flux noise of $1.3\mu\Phi_0$ Hz$^{-1/2}$. All chips were installed inside the mixing chamber of a $^3$He–$^4$He dilution refrigerator, which allows performing experiments at very low temperatures, between 0.013 K and 2 K.

### Theoretical methods

**Computational details.** Wavefunction-based calculations were carried out on molecular structures of the **[Dy$_2$]** and **[LaDy]** complexes by using the SA-CASSCF/RASSI-SO approach, as implemented in the OpenMolcas quantum chemistry package (version 22.10).[45,46] In this approach, the relativistic effects are treated in two steps on the basis of the Douglas–Kroll Hamiltonian. First, the scalar terms were included in the basis-set generation and were used to determine the spin-free wavefunctions and energies in the complete active space self-consistent field (CASSCF) method.[47] Next, spin–orbit coupling was added within the restricted-active-space-state-interaction (RASSI-SO) method, which uses the spin-free wavefunctions as basis states.[48] Spin–orbit (SO) integrals are calculated using the AMFI (atomic mean-field integrals) approximation.[49] The resulting wavefunctions and energies are used to compute the magnetic properties and $g$-tensors of the lowest states from the energy spectrum by using the pseudo-spin $S = 1/2$ formalism in the SINGLE-ANISO routine.[20,50] Cholesky decomposition of the bielectronic integrals was employed to save disk space and speed up the calculations.[51] For **[Dy$_2$]** and **[LaDy]**, the active space of the self-consistent field (CASSCF) method consisted of the nine 4f electrons of the Dy(III) ion spanning the seven 4f orbitals, *i.e.* CAS(9,7)SCF. State-averaged CASSCF calculations were performed for all of the sextets (21 roots), all of the quadruplets (224 roots), and 300 out of the 490 doublets (due to software limitations) of the Dy(III) ion. Twenty-one sextets, 128 quadruplets, and 107 doublets were mixed through spin–orbit coupling in RASSI-SO. All atoms were described by ANO-RCC basis sets.[52] The following contractions were used: [8s7p4d3f2g1h] for Dy, [8s7p5d2f] for La, [7s6p4d2f] for Y, [5s4p2d] for the Cl atom, [4s3p2d] for the O and N atoms of the first coordination sphere of the metal ions, [3s2p] for the C and the other O and N atoms and [2s] for the H atoms. The atomic positions were extracted from the X-ray crystal structures. Only the positions of the H atoms were optimized on

 

the Y(III) parent complexes with the Gaussian 16 (revision A.03) package[53] employing the PBE0 hybrid functional.[54] The "Stuttgart/Dresden" basis sets and effective core potentials were used to describe the yttrium atom,[55] whereas all other atoms were described with the SVP basis sets.[56]

## Author contributions

VV, DA, LAB and GA synthesized the molecular samples. OR performed and analysed the X-ray diffraction experiments. OR, DG and FL performed and analysed the magnetic and thermal characterization measurements. OR and JIM performed and analysed the EPR experiments. DD and TS designed and fabricated the micro-SQUID sensors. MCP and AL patterned the molecules by DPN and characterized the deposits *via* AFM and other techniques. AR, DG, JS and FL carried out the micro-SQUID experiments and analysed the results. MJMP performed the simulations of the flux coupled to the micro-SQUIDs. BLG performed the *ab initio* numerical calculations. GA and FL wrote the manuscript with contributions from all co-authors.

## Data availability

Crystallographic data can be found in CCDC 2310387 (**[$Dy_2$]**) and 2310388 (**[LaDy]**).†

Data shown in the main text figures are deposited at the FATMOLS community in the ZENODO repository: **https://zenodo.org/communities/fatmols-fet-open-862893/records?q=&l=list&p=1&s=10&sort=newest**.

## Conflicts of interest

There are no conflicts to declare.

## Acknowledgements

We acknowledge support from grants PID2022-140923NB-C21, PID2020-118329RB-I00 and PID2022-137764OB-I00, funded by MCIN/AEI/10.13039/501100011033 and by "ERDF A way of making Europe", from grants TED2021-131447B-C21, TED2021-129214B-I00 and PDC2022-133184-I00, funded by MCIN/AEI/10.13039/501100011033 and by the European Union NextGenerationEU/PRTR, from "Plan Complementario en Comunicación Cuántica" (PRTR-C17.I1) and "Plan Complementario en Materiales Avanzados", funded by Generalitat de Catalunya, Gobierno de Aragón and the European Union NextGenerationEU/PRTR, from the Gobierno de Aragón (DGA consolidated groups QMAD E09-23R and PLATON E31-23R), and from the CSIC Quantum Technology Platform PT-001. B. L. G. thanks the French GENCI/IDRIS-CINES centers for high-performance computing resources.

## References

1 (*a*) M. N. Leuenberger and D. Loss, *Nature*, 2001, **410**, 789; (*b*) F. Troiani and M. Affronte, *Chem. Soc. Rev.*, 2011, **40**, 3119; (*c*) G. Aromí, D. Aguilà, P. Gamez, F. Luis and O. Roubeau, *Soc. Rev.*, 2012, **41**, 537; (*d*) A. Gaita-Ariño, F. Luis, S. Hill and E. Coronado, *Nat. Chem.*, 2019, **11**, 301; (*e*) M. Atzori and R. Sessoli, *J. Am. Chem. Soc.*, 2019, **141**, 11339–11352; (*f*) M. R. Wasielewski, *et al.*, *Nat. Rev. Chem.*, 2020, **4**, 490.

2 (*a*) A. Ardavan, O. Rival, J. Morton, S. Blundell, A. Tyryshkin, G. Timco and R. E. P. Winpenny, *Phys. Rev. Lett.*, 2007, **98**, 057201; (*b*) C. J. Wedge, G. A. Timco, E. T. Spielberg, R. E. George, F. Tuna, S. Rigby, E. J. L. McInnes, R. E. P. Winpenny, S. J. Blundell and A. Ardavan, *Phys. Rev. Lett.*, 2012, **108**, 107204.

3 K. Bader, D. Dengler, S. Lenz, B. Endeward, S.-D. Jiang, P. Neugebauer and J. van Slageren, *Nat. Commun.*, 2014, **5**, 5304.

4 (*a*) J. M. Zadrozny, J. Niklas, O. G. Poluektov and D. E. Freedman, *ACS Cent. Sci.*, 2015, **1**, 488; (*b*) C.-J. Yu, M. J. Graham, J. M. Zadrozny, J. Niklas, M. D. Krzyaniak, M. R. Wasielewski, O. G. Poluektov and D. E. Freedman, *J. Am. Chem. Soc.*, 2016, **138**, 14678.

5 M. Atzori, E. Morra, L. Tesi, A. Albino, M. Chiesa, L. Sorace and R. Sessoli, *J. Am. Chem. Soc.*, 2016, **138**, 11234.

6 S. Carretta, D. Zueco, A. Chiesa, Á. Gómez-León and F. Luis, *Appl. Phys. Lett.*, 2021, **118**, 240501.

7 (*a*) F. Luis, A. Repollés, M. J. Martínez-Pérez, D. Aguilà, O. Roubeau, D. Zueco, P. J. Alonso, M. Evangelisti, A. Camón, J. Sesé, L. A. Barrios and G. Aromí, *Phys. Rev. Lett.*, 2011, **107**, 117203; (*b*) D. Aguilà, D. Barrios, V. Velasco, O. Roubeau, A. Repollés, P. J. Alonso, J. Sesé, S. Teat, F. Luis and G. Aromí, *J. Am. Chem. Soc.*, 2014, **136**, 14215; (*c*) F. Luis, P. J. Alonso, O. Roubeau, V. Velasco, D. Zueco, D. Aguilà, J. I. Martínez, L. A. Barrios and G. Aromí, *Commun. Chem.*, 2020, **3**, 176; (*d*) E. Macaluso, M. Rubín, D. Aguilà, A. Chiesa, J. I. Martínez, L. A. Barrios, P. J. Alonso, O. Roubeau, F. Luis, G. Aromí and S. Carretta, *Chem. Sci.*, 2020, **11**, 10337.

8 (*a*) A. Ardavan, A. M. Bowen, A. Fernández, A. J. Fielding, D. Kaminski, F. Moro, C. A. Muryn, M. D. Wise, A. Ruggi, E. J. L. McInnes, K. Severin, G. Timco, F. Tuna, G. F. S. Whitehead and R. E. P. Winpenny, *npj Quantum Inf.*, 2015, **1**, 15012; (*b*) J. Ferrando-Soria, E. Moreno-Pineda, A. Chiesa, A. Fernández, S. A. Magee, S. Carretta, P. Santini, I. Vitorica-Yrezabal, F. Tuna, G. Timco, E. J. L. McInness and R. E. P. Winpenny, *Nat. Commun.*, 2016, **7**, 11377; (*c*) A. Fernández, J. Ferrando-Soria, E. Moreno-Pineda, F. Tuna, I. J. Vitorica-Yrezabal, C. Knappke, J. Ujma, C. A. Muryn, G. A. Timco, P. E. Barran, A. Ardavan and R. E. P. Winpenny, *Nat. Commun.*, 2016, **7**, 10240.

9 M. D. Jenkins, Y. Duan, B. Diosdado, J. J. García-Ripoll, A. Gaita-Ariño, C. Giménez-Saiz, P. J. Alonso, E. Coronado and F. Luis, *Phys. Rev. B*, 2017, **95**, 064423.

10 (*a*) E. Moreno-Pineda, M. Damjanovic, O. Fuhr, W. Wernsdorfer and M. Ruben, *Angew. Chem., Int. Ed.*, 2017, **56**, 9915; (*b*) E. Moreno-Pineda, C. Godfrin, F. Balestro, W. Wernsdorfer and M. Ruben, *Chem. Soc. Rev.*, 2018, **47**, 501; (*c*) C. Godfrin, A. Ferhat, R. Ballou, S. Klyatskaya, M. Ruben, W. Wernsdorfer and F. Balestro, *Phys. Rev. Lett.*, 2017, **119**, 187702.

11 (*a*) R. Hussain, G. Allodi, A. Chiesa, E. Garlatti, D. Mitcov, A. Konstantatos, K. S. Pedersen, R. De Renzi, S. Piligkos and S. Carretta, *J. Am. Chem. Soc.*, 2018, **140**, 9814; (*b*) I. Gimeno, A. Urtizberea, J. Román-Roche, D. Zueco, A. Camón, P. J. Alonso, O. Roubeau and F. Luis, *Chem. Sci.*, 2021, **12**, 5621; (*c*) S. Chicco, A. Chiesa, G. Allodi, E. Garlatti, M. Atzori, L. Sorace, R. De Renzi, R. Sessoli and S. Carretta, *Chem. Sci.*, 2021, **12**, 12046.

12 B. P. Lanyon, M. Barbieri, M. P. Alemida, T. Jenewein, T. C. Ralph, K. J. Resch, G. J. Pryde, J. L. O'Brien, A. Gilchrist and A. G. White, *Nat. Phys.*, 2009, **5**, 134.

13 A. Chiesa, E. Macaluso, F. Petiziol, S. Wimberger, P. Santini and S. Carretta, *J. Phys. Chem. Lett.*, 2020, **11**, 8610.

14 M. D. Jenkins, T. Hümmer, M. J. Martínez-Pérez, J. J. García-Ripoll, D. Zueco and F. Luis, *New J. Phys.*, 2013, **15**, 095007.

15 M. D. Jenkins, D. Zueco, O. Roubeau, G. Aromí, J. Majer and F. Luis, *Dalton Trans.*, 2016, **45**, 16682.

16 A. Chiesa, S. Roca, S. Chicco, M. de Ory, A. Gómez-León, A. Gomez, D. Zueco, F. Luis and S. Carretta, *Phys. Rev. Appl.*, 2023, **19**, 064060.

17 A. Urtizberea, E. Natividad, P. J. Alonso, L. Pérez-Martínez, M. A. Andrés, I. Gascón, I. Gimeno, F. Luis and O. Roubeau, *Mater. Horiz.*, 2020, **7**, 885.

18 I. Gimeno, W. Kersten, M. C. Pallarés, P. Hermosilla, M. J. Martínez-Pérez, M. D. Jenkins, A. Angerer, C. Sánchez-Azqueta, D. Zueco, J. Majer, A. Lostao and F. Luis, *ACS Nano*, 2020, **14**, 8707.

19 L. Malavolti, M. Briganti, M. Hänze, G. Serrano, I. Cimatti, G. McMurtrie, E. Otero, P. Ohresser, F. Totti, M. Mannini, R. Sessoli and S. Loth, *Nano Lett.*, 2018, **18**(12), 7955.

20 D. Aguilà, L. A. Barrios, F. Luis, A. Repollés, O. Roubeau, S. J. Teat and G. Aromí, *Inorg. Chem.*, 2010, **49**, 6784.

21 D. Aguilà, L. A. Barrios, V. Velasco, L. Arnedo, N. Aliaga-Alcalde, M. Menelaou, S. J. Teat, O. Roubeau, F. Luis and G. Aromí, *Chem. – Eur. J.*, 2013, **19**, 5881.

22 J. Gónzalez-Fabra, N. A. G. Bandeira, V. Velasco, L. A. Barrios, D. Aguilà, S. J. Teat, O. Roubeau, C. Bo and G. Aromí, *Chem. – Eur. J.*, 2017, **23**, 5117.

23 D. Aguilà, V. Velasco, L. A. Barrios, J. González-Fabra, C. Bo, S. J. Teat, O. Roubeau and G. Aromí, *Inorg. Chem.*, 2018, **57**, 8429.

24 (*a*) M. J. Martínez-Pérez, J. Sesé, F. Luis, D. Drung and T. Schurig, *Rev. Sci. Instrum.*, 2010, **81**, 016108; (*b*) M. J. Martínez-Pérez, E. Bellido, R. de Miguel, J. Sesé, A. Lostao, C. Gómez-Moreno, D. Drung, T. Schurig, D. Ruiz-Molina and F. Luis, *Appl. Phys. Lett.*, 2011, **99**, 032504.

25 E. Bellido, P. González-Monje, A. Repollés, M. D. Jenkins, J. Sesé, D. Drung, T. Schurig, K. Awaga, F. Luis and D. Ruiz-Molina, *Nanoscale*, 2013, **5**, 12565.

26 E. Bartolomé, P. J. Alonso, A. Arauzo, J. Luzón, J. Bartolomé, C. Racles and C. Turta, *Dalton Trans.*, 2012, **41**, 10382.

27 E. Moreno-Pineda, N. F. Chilton, R. Marx, M. Dörfel, D. O. Sells, P. Neugebauer, S.-D. Jiang, D. Collison, J. van Slageren, E. J. L. McInnes and R. E. P. Winpenny, *Nat. Commun.*, 2014, **5**, 5243.

28 R. D. Piner, J. Zhu, F. Xu, S. Hong and C. A. Mirkin, *Science*, 1999, **283**, 661.

29 E. Bellido, R. de Miguel, D. Ruiz-Molina, A. Lostao and D. Maspoch, *Adv. Mater.*, 2010, **22**, 352.

30 K. S. Cole and R. H. Cole, *J. Chem. Phys.*, 1941, **9**, 341.

31 N. V. Prokof'ev and P. C. E. Stamp, *Phys. Rev. Lett.*, 1998, **80**, 5794.

32 J. F. Fernández, *Phys. Rev. B: Condens. Matter Mater. Phys.*, 2002, **66**, 064423.

33 F. Luis, M. J. Martínez-Pérez, O. Montero, E. Coronado, S. Cardona-Serra, C. Martí-Gastaldo, J. M. Clemente-Juan, J. Sesé, D. Drung and T. Schurig, *Phys. Rev. B: Condens. Matter Mater. Phys.*, 2010, **82**, 060403(R).

34 G. M. Sheldrick, *Acta Crystallogr., Sect. A: Found. Adv.*, 2015, **71**, 3–8.

35 G. M. Sheldrick, *Acta Crystallogr., Sect. C: Struct. Chem.*, 2015, **71**, 3–8.

36 A. L. Spek, *Acta Crystallogr., Sect. C: Struct. Chem.*, 2015, **71**, 9–18.

37 A. L. Spek, *Acta Crystallogr., Sect. C: Struct. Chem.*, 2015, **71**, 9–18.

38 I. Horcas, R. Fernández, J. M. Gómez-Rodríguez, J. Colchero, J. Gómez-Herrero and A. M. Baró, *Rev. Sci. Instrum.*, 2007, **78**, 013705.

39 R. Bachmann, F. J. DiSalvo Jr., T. H. Geballe, R. L. Greene, R. E. Howard, C. N. King, H. C. Kirsch, K. N. Lee, R. E. Schwall, H.-U. Thomas and R. B. Zubeck, *Rev. Sci. Instrum.*, 1972, **43**, 205.

40 M. Evangelisti, F. Luis, L. J. de Jongh and M. Affronte, *J. Mater. Chem.*, 2006, **16**, 2534–2549.

41 S. Stoll and A. Schweiger, *J. Magn. Reson.*, 2006, **178**, 42–55.

42 M. J. Martínez-Pérez, J. Sesé, F. Luis, D. Drung and T. Schurig, *Rev. Sci. Instrum.*, 2010, **81**, 016108.

43 M. J. Martínez-Pérez, J. Sesé, F. Luis, R. Córdoba, D. Drung, T. Schurig, E. Bellido, R. de Miguel, C. Gómez-Moreno, A. Lostao and D. Ruiz-Molina, *IEEE Trans. Appl. Supercond.*, 2011, **21**, 345.

44 D. Drung, J.-H. Storm, F. Ruede, A. Kirste, M. Regin, T. Schurig, A. M. Repollés, J. Sesé and F. Luis, *IEEE Trans. Appl. Supercond.*, 2014, **24**, 1.

45 F. Aquilante, L. De Vico, N. Ferré, G. Ghigo, P.-A. Malmqvist, P. Neograd y, T. B. Pedersen, M. Pitonak, M. Reiher, B. O. Roos, L. Serrano-Andrés, M. Urban, V. Veryazov and R. Lindh, *J. Comput. Chem.*, 2010, **31**, 224.

46 I. F. Galván, M. Vacher, A. Alavi, C. Angeli, F. Aquilante, J. Autschbach, J. J. Bao, S. I. Bokarev, N. A. Bogdanov, R. K. Carlson, L. F. Chibotaru, J. Creutzberg, N. Dattani, M. G. Delcey, S. S. Dong, A. Dreuw, L. Freitag, L. M. Frutos, L. Gagliardi, F. Gendron, A. Giussani, L. González, G. Grell,

 

M. Guo, C. E. Hoyer, M. Johansson, S. Keller, S. Knecht, G. Kovačević, E. Källman, G. Li Manni, M. Lundberg, Y. Ma, S. Mai, J. P. Malhado, P.Å Malmqvist, P. Marquetand, S. A. Mewes, J. Norell, M. Olivucci, M. Oppel, Q. M. Phung, K. Pierloot, F. Plasser, M. Reiher, A. M. Sand, I. Schapiro, P. Sharma, C. J. Stein, L. K. Sørensen, D. G. Truhlar, M. Ugandi, L. Ungur, A. Valentini, S. Vancoillie, V. Veryazov, O. Weser, T. A. Wesołowski, P.-O. Widmark, S. Wouters, A. Zech, J. P. Zobel and R. Lindh, *J. Chem. Theory Comput.*, 2019, **15**, 5925.

47 B. O. Roos, P. R. Taylor and P. E. M. Siegbahn, *Chem. Phys.*, 1980, **48**, 157.

48 (*a*) P. A. Malmqvist, B. O. Roos and B. Schimmelpfennig, *Chem. Phys. Lett.*, 2002, **357**, 230–240; (*b*) P.-A. Malmqvist and B. O. Roos, *Chem. Phys. Lett.*, 1989, **155**, 189.

49 B. A. Heß, C. M. Marian, U. Wahlgren and O. Gropen, *Chem. Phys. Lett.*, 1996, **251**, 365.

50 (*a*) L. F. Chibotaru and L. Ungur, *J. Chem. Phys.*, 2012, **137**, 064112; (*b*) L. F. Chibotaru, L. Ungur and A. Soncini, *Angew. Chem., Int. Ed.*, 2008, **47**, 4126.

51 F. Aquilante, P. A. Malmqvist, T. B. Pedersen, A. Ghosh and B. O. Roos, *J. Chem. Theory Comput.*, 2008, **4**, 694.

52 (*a*) B. O. Roos, R. Lindh, P. A. Malmqvist, V. Veryazov and P. O. Widmark, *J. Phys. Chem. A*, 2004, **108**, 2851; (*b*) B. O. Roos, R. Lindh, P. A. Malmqvist, V. Veryazov, P. O. Widmark and A. C. Borin, *J. Phys. Chem. A*, 2008, **112**, 11431.

53 M. J. Frisch, G. W. Trucks, H. B. Schlegel, G. E. Scuseria, M. A. Robb, J. R. Cheeseman, G. Scalmani, V. Barone, G. A. Petersson, H. Nakatsuji, X. Li, M. Caricato, A. V. Marenich, J. Bloino, B. G. Janesko, R. Gomperts, B. Mennucci, H. P. Hratchian, J. V. Ortiz, A. F. Izmaylov, J. L. Sonnenberg, D. Williams-Young, F. Ding, F. Lipparini, F. Egidi, J. Goings, B. Peng, A. Petrone, T. Henderson, D. Ranasinghe, V. G. Zakrzewski, J. Gao, N. Rega, G. Zheng, W. Liang, M. Hada, M. Ehara, K. Toyota, R. Fukuda, J. Hasegawa, M. Ishida, T. Nakajima, Y. Honda, O. Kitao, H. Nakai, T. Vreven, K. Throssell, J. A. Montgomery Jr., J. E. Peralta, F. Ogliaro, M. J. Bearpark, J. J. Heyd, E. N. Brothers, K. N. Kudin, V. N. Staroverov, T. A. Keith, R. Kobayashi, J. Normand, K. Raghavachari, A. P. Rendell, J. C. Burant, S. S. Iyengar, J. Tomasi, M. Cossi, J. M. Millam, M. Klene, C. Adamo, R. Cammi, J. W. Ochterski, R. L. Martin, K. Morokuma, O. Farkas, J. B. Foresman and D. J. Fox, Gaussian, Inc., Wallingford CT, 2016.

54 (*a*) J. P. Perdew, K. Burke and M. Ernzerhof, *Phys. Rev. Lett.*, 1996, **77**, 3865; (*b*) C. Adamo and V. Barone, *J. Chem. Phys.*, 1999, **110**, 6158.

55 M. Dolg, H. Stoll and H. Preuss, *Theor. Chim. Acta*, 1993, **85**, 441.

56 F. Weigend and R. Ahlrichs, *Phys. Chem. Chem. Phys.*, 2005, **7**, 3297.

Supporting information for manuscript

# Asymmetric [$Dy_2$] molecules deposited into micro-SQUID susceptometers: in-situ characterization of their magnetic integrity

Ana Repollés,[a,†] María Carmen Pallarés,[a,b,†] David Aguilà,[c,d] Olivier Roubeau,[a] Verónica Velasco,[c,d] Diego Gella,[a] Leoní A. Barrios,[c,d] María José Martínez-Pérez,[a] Javier Sesé,[a] Dietmar Drung,[e] Jesús Ignacio Martínez,[a] Thomas Schurig,[e] Boris Le Guennic,[f] Anabel Lostao,[a,b,g] Guillem Aromí,[c,d] and Fernando Luis[a]

[a]*Instituto de Nanociencia y Materiales de Aragón (INMA), CSIC and Universidad de Zaragoza, Plaza San Francisco s/n, 50009 Zaragoza, Spain. Email: fluis@unizar.es*
[b]*Laboratorio de Microscopias Avanzadas (LMA), Universidad de Zaragoza, 50018 Zaragoza, Spain*
[c]*Departament de Química Inorgànica i Orgànica, Universitat de Barcelona, Diagonal 645, 08028 Barcelona, Spain. E-mail: aromi@ub.edu*
[d]*Institut of Nanoscience and Nanotechnology of the University of Barcelona (IN2UB), Barcelona, Spain.*
[e]*Physikalisch-Technische Bundesanstalt (PTB), Abbestraße 2-12, D-10587 Berlin, Germany*
[f]*Univ Rennes, CNRS, ISCR (Institut des Sciences Chimiques de Rennes) - UMR 6226, F-35000 Rennes, France*
[g]*Fundación ARAID, 50018 Zaragoza, Spain*

## Table of contents

## 1. Supporting tables and figures

**Table S1.** Crystallographic and refinement parameters for **[$Dy_2$]** and **[LaDy]**.

| Compound | **[$Dy_2$]** | **[LaDy]** |
|---|---|---|
| Crystal size ($mm^3$) | 0.12x0.10x0.09 | 0.23x0.05x0.02 |
| Formula | $C_{55}H_{37}ClDy_2N_5O_{15}$, 3($C_5H_5N$), $C_5H_6N$ | $C_{50}H_{35}DyLaN_5O_{19}$, 4($C_5H_5N$), $C_5H_6N$ |
| FW (g $mol^{-1}$) | 1685.75 | |
| Wavelength (Å) | 0.71073 | 0.71073 |
| Crystal system | monoclinic | monoclinic |
| Space group | $P2_1/n$ | $P2_1/n$ |
| $Z$ | 4 | 4 |
| $T$ (K) | 150(2) | 150(2) |
| $a$ (Å) | 12.7916(4) | 14.533(4) |
| $b$ (Å) | 16.6444(4) | 15.8767(13) |
| $c$ (Å) | 32.5450(10) | 32.939(4) |
| $\beta$ (°) | 97.104(3) | 91.083(15) |
| $V$ ($Å^3$) | 6875.9(3) | 7599(2) |
| $\rho_{calcd}$ (g $cm^{-3}$) | 1.628 | 1.593 |
| $\mu$ ($mm^{-1}$) | 2.271 | 1.612 |
| Independent reflections | 9873 ($R_{int}$ = 0.1261) | 6864 ($R_{int}$ = 0.1282) |
| restraints / parameters | 102 / 919 | 359 / 937 |
| Goodness-of-fit on $F^2$ | 1.026 | 1.010 |
| Final $R_1$ / w$R_2$ [$I>2\sigma(I)$] | 0.0578 / 0.0976 | 0.0611 / 0.1160 |
| Final $R_1$ / w$R_2$ [all data] | 0.1056 / 0.1126 | 0.1285 / 0.1535 |
| largest diff. peak and hole ($e$ $Å^3$) | 1.031 / –0.757 | 0.862 / –0.789 |

**Table S2.** Metal–ligand bond distances (Å) and metal···metal separations (Å) in the structures of compounds **[$Dy_2$]** and **[LaDy]**.

| **[$Dy_2$]** | | **[LaDy]** | |
|---|---|---|---|
| Dy1–O3 | 2.301(6) | Dy1–O11 | 2.358(10) |
| Dy1–O11 | 2.310(6) | Dy1–O9 | 2.373(10) |
| Dy1–O9 | 2.343(6) | Dy1–O4 | 2.436(11) |
| Dy1–O8 | 2.398(5) | Dy1–O19 | 2.444(10) |
| Dy1–O4 | 2.405(6) | Dy1–O8 | 2.450(10) |
| Dy1–O13 | 2.416(6) | Dy1–O13 | 2.453(8) |
| Dy1–N3 | 2.490(7) | Dy1–N3 | 2.482(11) |
| Dy1–N4 | 2.633(8) | Dy1–N5 | 2.711(12) |
| Dy1–N5 | 2.653(8) | La2–O14 | 2.478(10) |
| Dy2–O6 | 2.363(6) | La2–O1 | 2.495(10) |
| Dy2–O1 | 2.371(6) | La2–O6 | 2.506(9) |
| Dy2–O13 | 2.385(6) | La2–O13 | 2.543(9) |
| Dy2–O14 | 2.404(6) | La2–O3 | 2.583(9) |
| Dy2–O3 | 2.494(6) | La2–N1 | 2.641(13) |
| Dy2–O8 | 2.518(6) | La2–O16 | 2.648(10) |
| Dy2–N1 | 2.534(7) | La2–O8 | 2.683(9) |
| Dy2–N2 | 2.537(7) | La2–N2 | 2.740(12) |
| Dy2–Cl1 | 2.725(2) | La2–O17 | 2.807(12) |
| | | | |
| Dy1···Dy2 | 3.7748(6) | Dy1···La2 | 3.8845(11) |

**Table S3.** Details of H-bonding interactions in the structures of compounds **[$Dy_2$]** and **[LaDy]**.

| D–H···A | D–H (Å) | H···A (Å) | D–A (Å) | D–H···A (º) |
|---|---|---|---|---|
| **[$Dy_2$]** | | | | |
| N1S–H1S···O1 | 0.88 | 2.23 | 2.940(12) | 137.6 |
| N1S–H1S···O1 | 0.88 | 2.15 | 2.924(12) | 146.9 |
| | | | | |
| **[LaDy]** | | | | |
| N1S–H1SB···O1 | 0.88 | 3.11 | 3.527(19) | 111.1 |
| O19–H19C···N2S | 0.90(2) | 2.02(4) | 2.771(17) | 141(6) |
| O19–H19D···N3S | 0.90(2) | 2.02(4) | 2.745(16) | 138(6) |

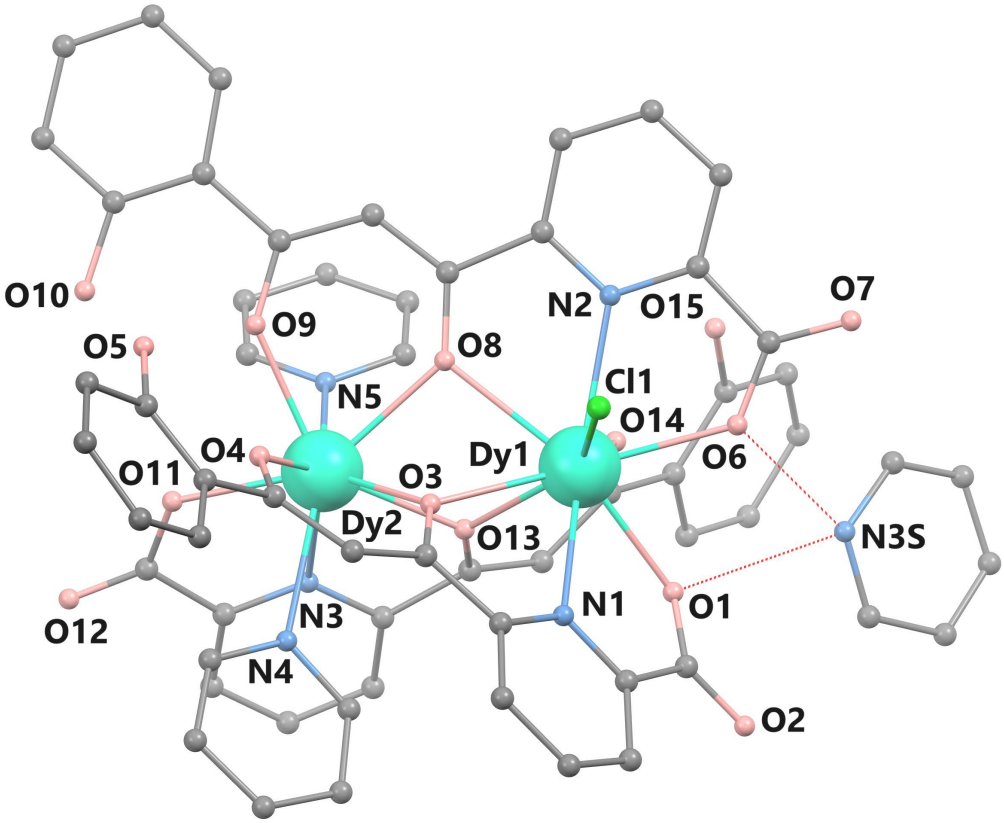


Figure S1. Molecular structure of **[$Dy_2$]** with heteroatoms labelled. Green is Dy, grey is C, salmon is O, blue is N. Hydrogen atoms are omitted for simplicity. Hydrogen bonds between $Hpy^+$ and the complex shown as are dashed red lines.

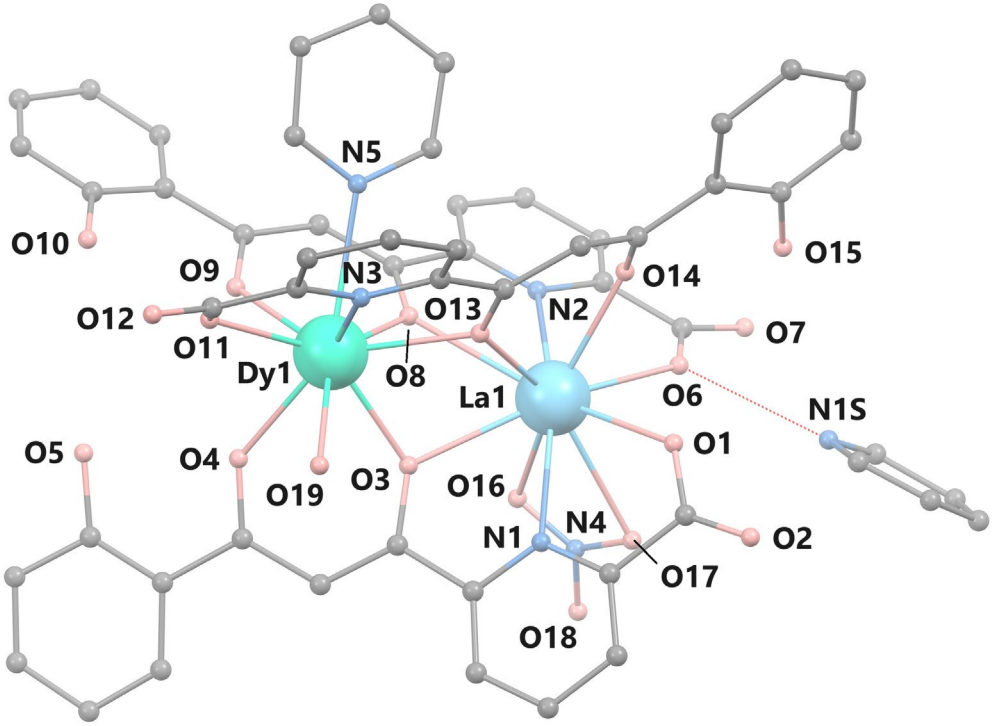


Figure S2. Molecular structure of **[LaDy]** with heteroatoms labelled. Green is Dy, light blue is La, grey is C, salmon is O, blue is N. Hydrogen atoms are omitted for simplicity. Hydrogen bonds between $Hpy^+$ and the complex shown as are dashed red lines.

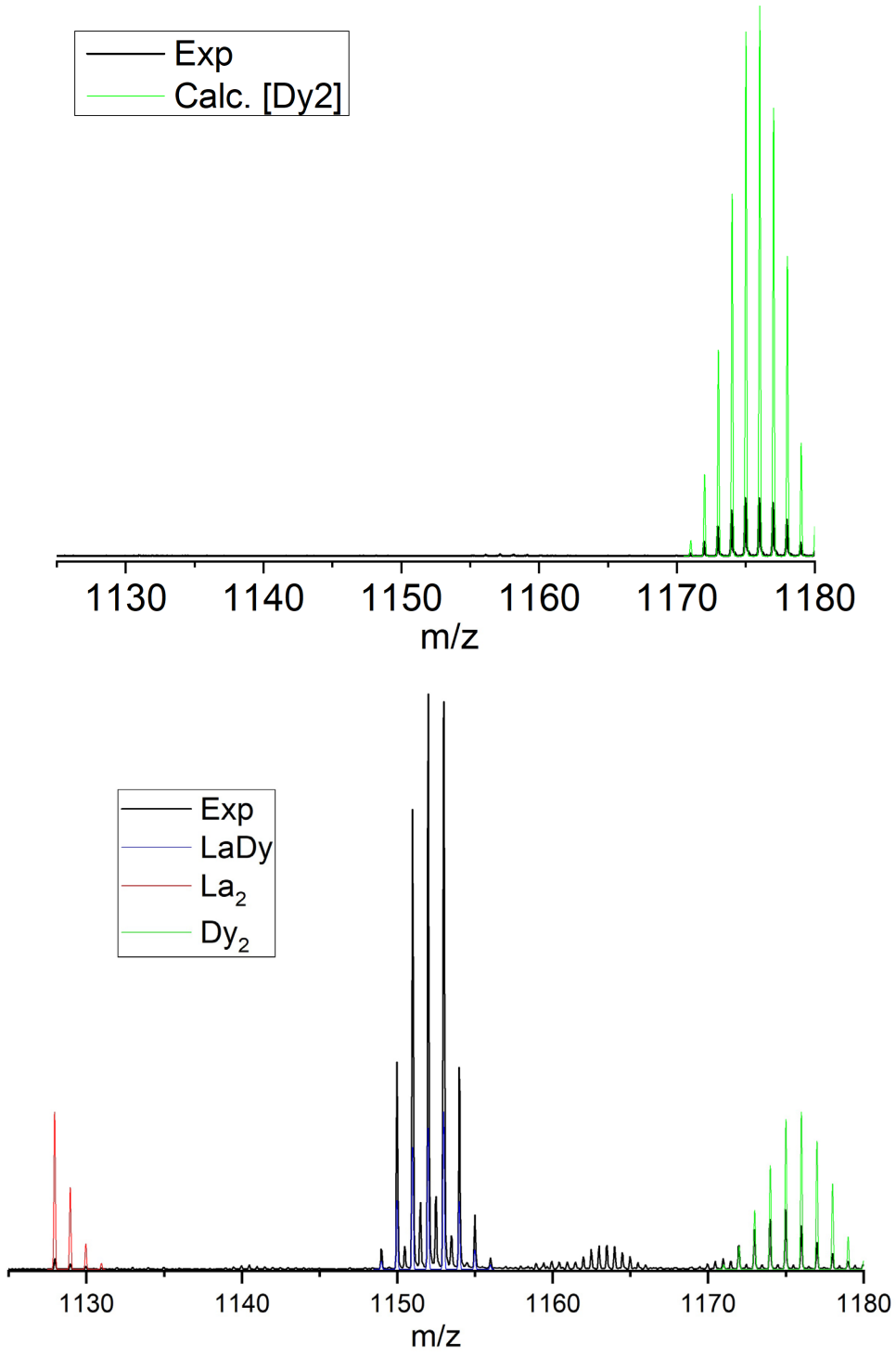


Figure S3. Top: Selected region of the experimental (black line) MALDI-TOF spectrogram of compound **[Dy$_2$]**, emphasizing the simulated ([$Dy_2(HL)_3$] + $H^+$)$^+$ (*m*/*z* = 1176.1010) fragment (green line). Bottom: Selected region of the experimental (black line) ESI-MS spectrogram of compound **[LaDy]**, emphasizing the simulated ([$LaDy(HL)_3$] + $H^+$)$^+$ (*m*/*z* = 1151.9956) fragment (blue line), together with the corresponding calculated signals for the **[Dy$_2$]** (green line) and **[La$_2$]** (red line), metal distributions. The minor traces of the homometallic moieties are due to scrambling taking place in the required methanol solution used for the mass spectrometry experiments (see also the bottom panel in Fig. S4 below).

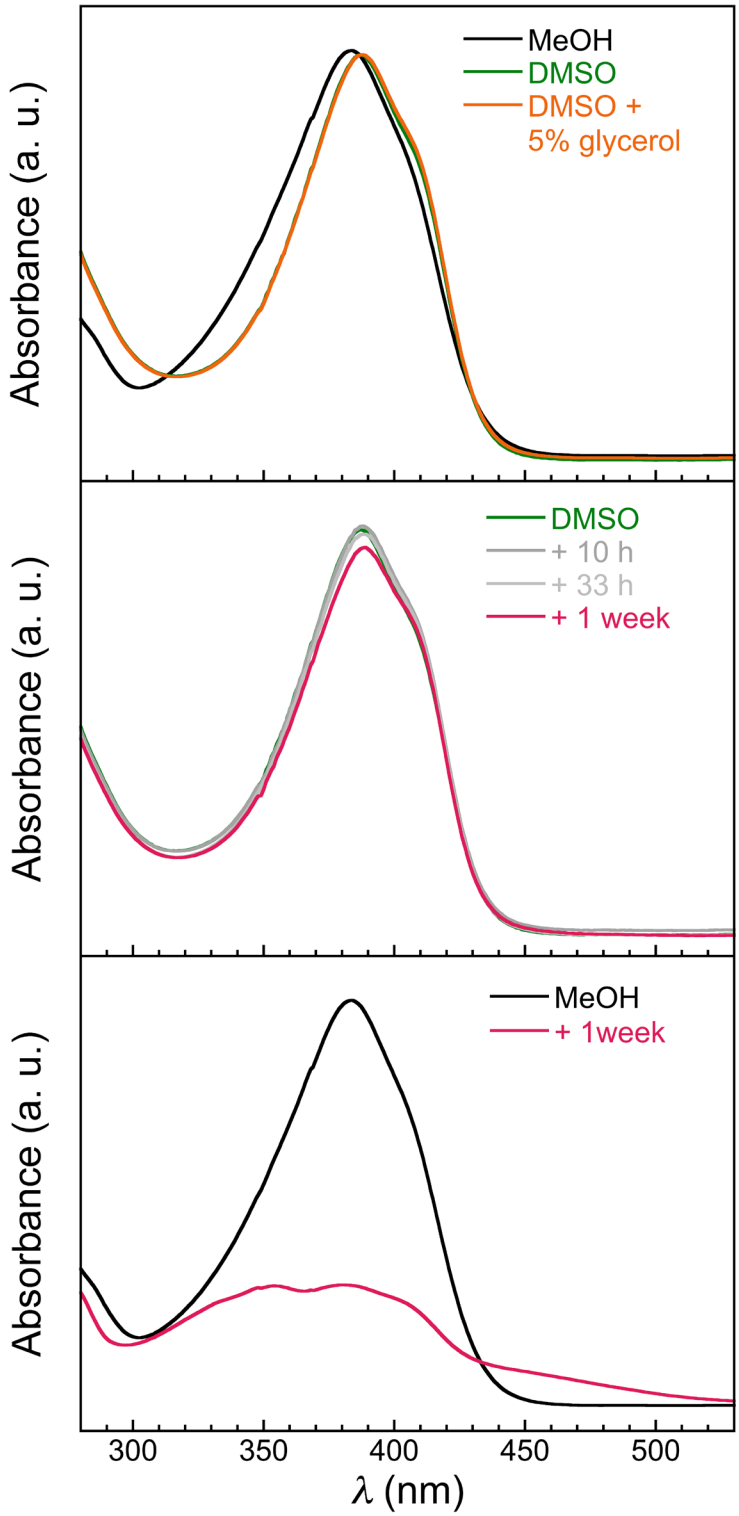


Figure S4. UV-visible absorption spectra for solutions of **[$Dy_2$]**: top, comparison of solutions in MeOH, DMSO and DMSO + 5% glycerol as indicated; middle and bottom, ageing of DMSO and MeOH solutions, respectively. “a.u” means arbitrary units.

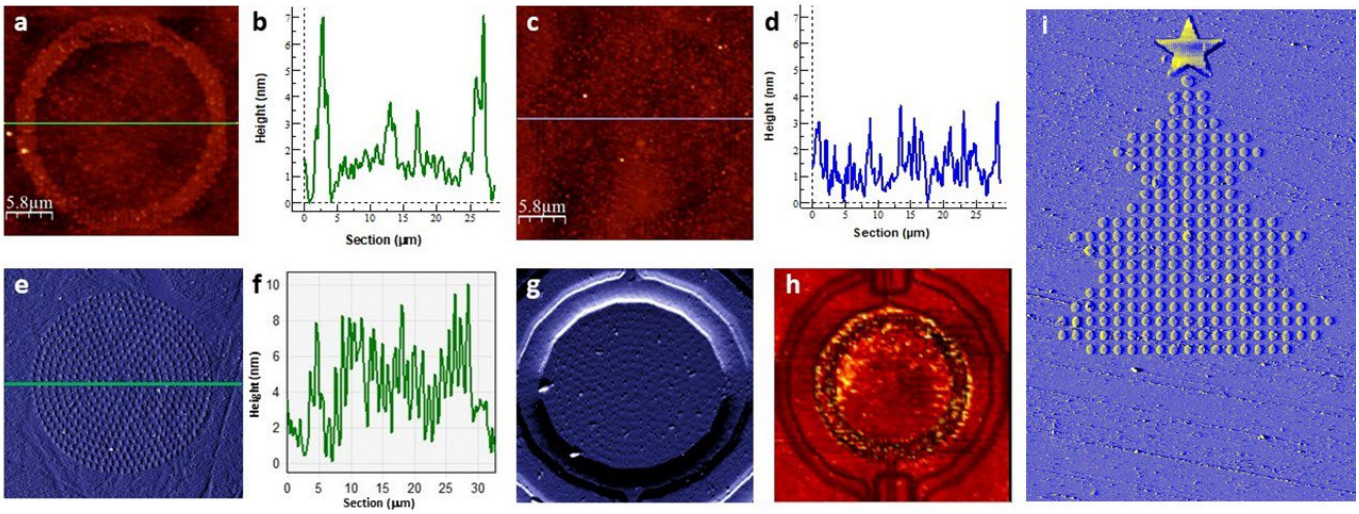


Figure S5. Controlled patterning of **[$Dy_2$]** nano- and micro-deposits by means of DPN nanolithography. a) AFM image of a 5-layer ring of **[$Dy_2$]** molecules patterned onto a silicon substrate. b) Height profile measured along the green line in the sample shown in a). c) AFM image of the same ring fabricated under the same experimental conditions as those used in a) with an ink that contains only the solvent and glycerol (i.e., no **[$Dy_2$]** molecules). d) Height profile measured along the blue line in the sample shown in c) showing that there is hardly any residue of glycerol. e) AFM 3-D topography image of a circle made of 5 nm (approximately 3 molecular layers) thick **[$Dy_2$]** dots, as shown in f) height profile corresponding to the green line exhibited in e). g) AFM 3-D topography image of the same pattern as in e) integrated inside the micro-SQUID pick-up coil. h) AFM 3-D topography image of 5-layer **[$Dy_2$]** dots patterned to form a ring next to the inner side of the micro-SQUID pickup coil under the same conditions as those used for a). i) Christmas tree fabricated organizing 5 nm thick **[$Dy_2$]** trilayers in 1.5 $\mu m^2$ wide dots. The star is a continuous 10 nm thick nanolitography.

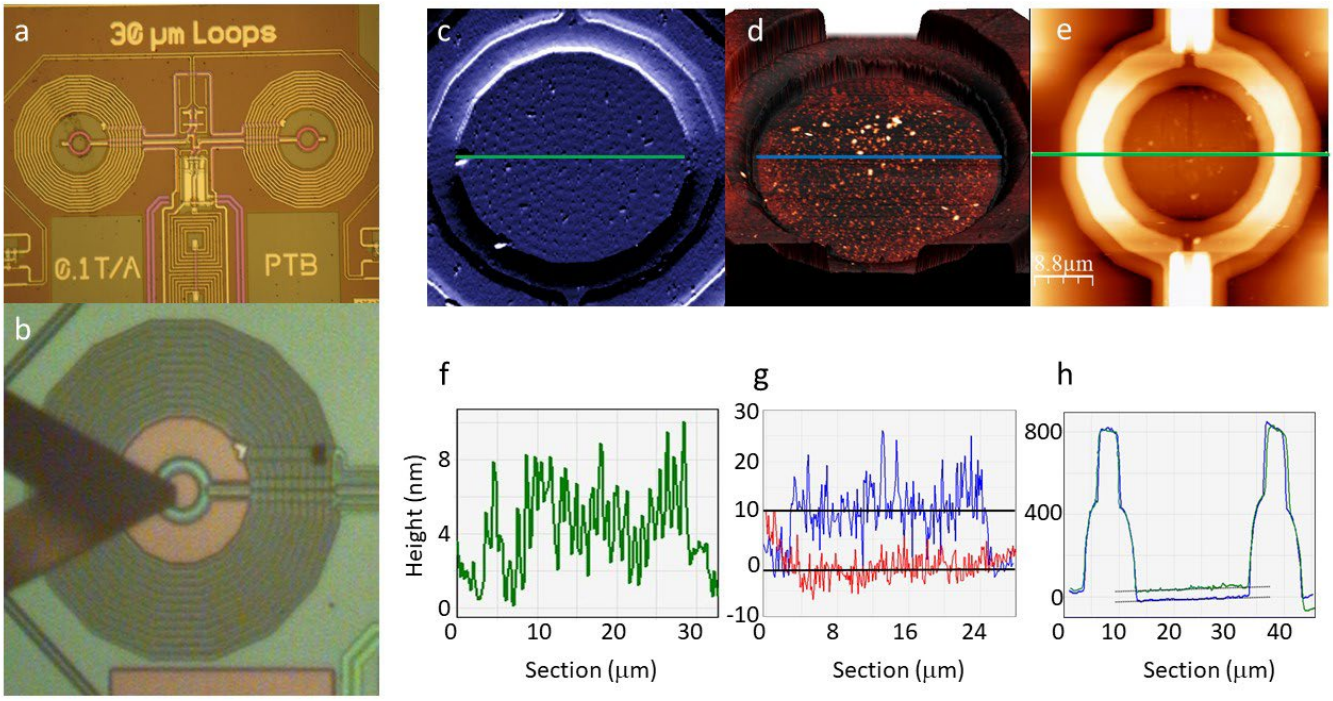


Figure S6. Integration of **[Dy$_2$]** deposits onto micro-SQUID susceptometers. (a) The micro-SQUID is made of two loops (coloured in magenta) with a gradiometric design, which act as pick-up coils. They are surrounded by two identical excitation coils that generate the ac magnetic field, perpendicular to the chip's surface. (b) Image of the AFM tip of the DPN system traversing the area defined by one of the two pick-up coils during one of the deposition processes. (c-e) and (f-h) Topography images (top) and height profiles along the corresponding lines at the top images (bottom) of three molecular deposits labelled as **[Dy$_2$]$_{DPN1}$** (c,f), **[Dy$_2$]$_{DPN2}$** (d,g) and **[Dy$_2$]$_{DPN3}$** (e,h). In (g) and (h) the lines below represent the profile of the substrate. The samples were made by successive coating and deposition steps. In the bigger samples, the large volume of the dots makes them merge on the substrate, forming a continuous thin film that covers the entire coil. Thus, deposition of approximately 3, 8 and 34 molecular layer thick deposits, were achieved respectively. The estimated number of **[Dy$_2$]** molecules transferred to the device is $2.3\times10^8$, $1.8\times10^9$ and $7\times10^9$, respectively.

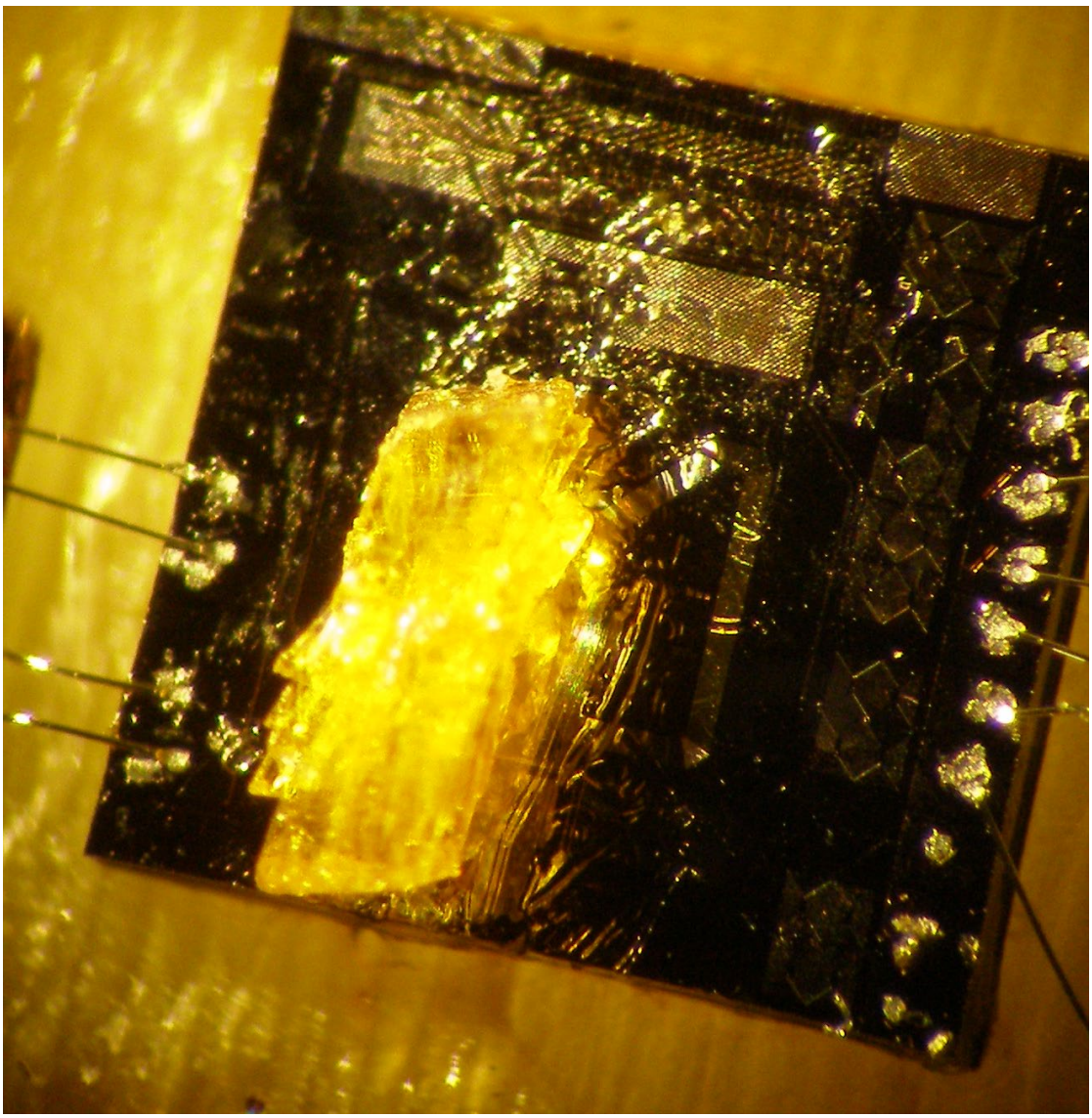

Figure S7. Optical microscopy image of a micro-SQUID susceptometer hosting a bulk **[$Dy_2$]** sample on one of its 800×400 $\mu m^2$ banana-shaped pick-up and excitation coils.

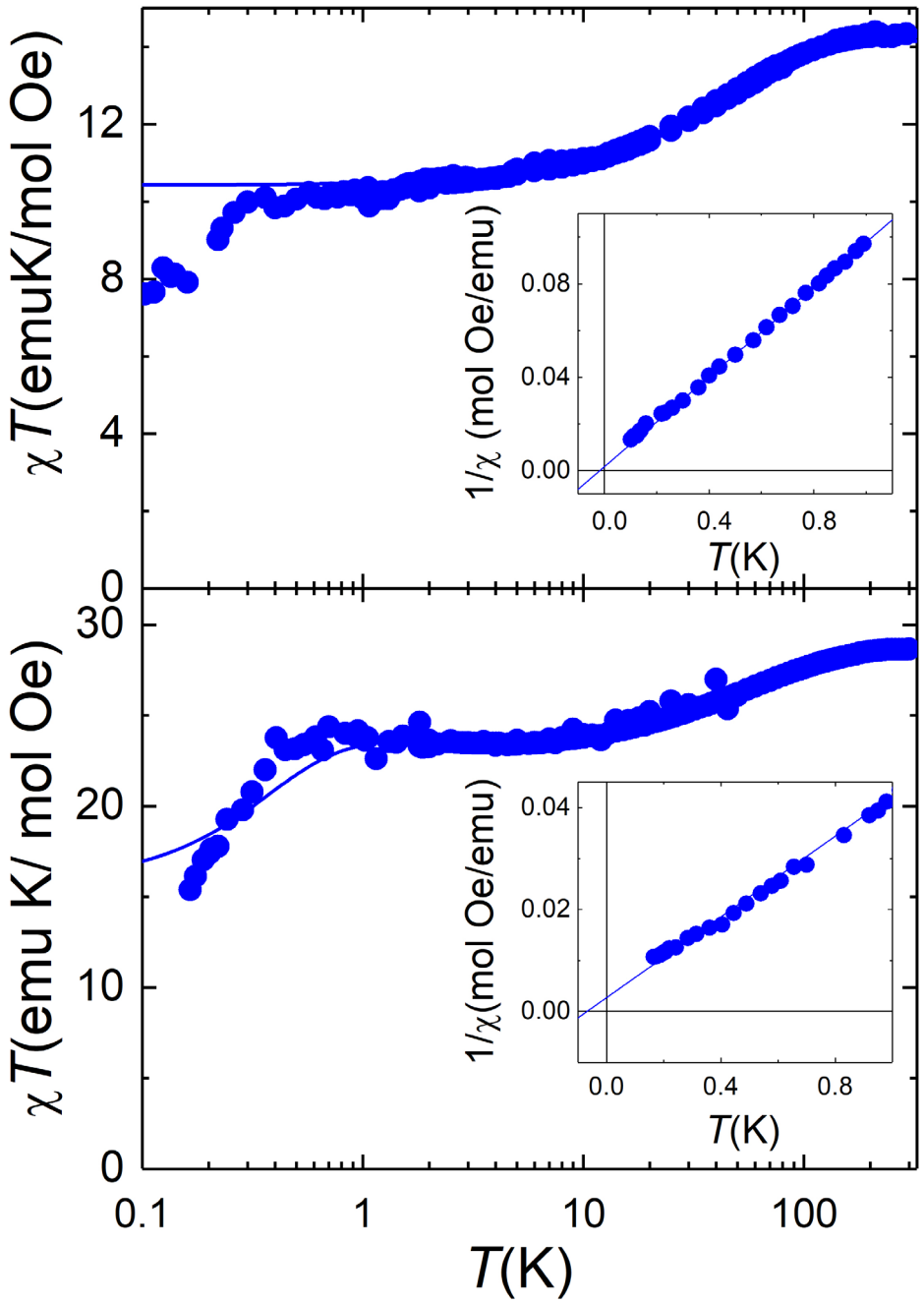


Figure S8. Comparison between the $\chi T$ products of bulk **[LaDy]** (top panel) and **[Dy$_2$]** (bottom panel). The data have been extracted from the magnetic susceptibility measured at sufficiently low frequencies and sufficiently high temperatures to be considered as the equilibrium linear response of each sample. The insets show the reciprocal equilibrium susceptibility measured below $T$ = 1 K (solid dots) and the Curie-Weiss fit (solid lines). The Weiss temperatures, which characterize the typical strength of spin-spin interactions, are $\theta$ = -0.015(5) K for **[LaDy]** and $\theta$ = -0.067(1) K for **[Dy$_2$]**.

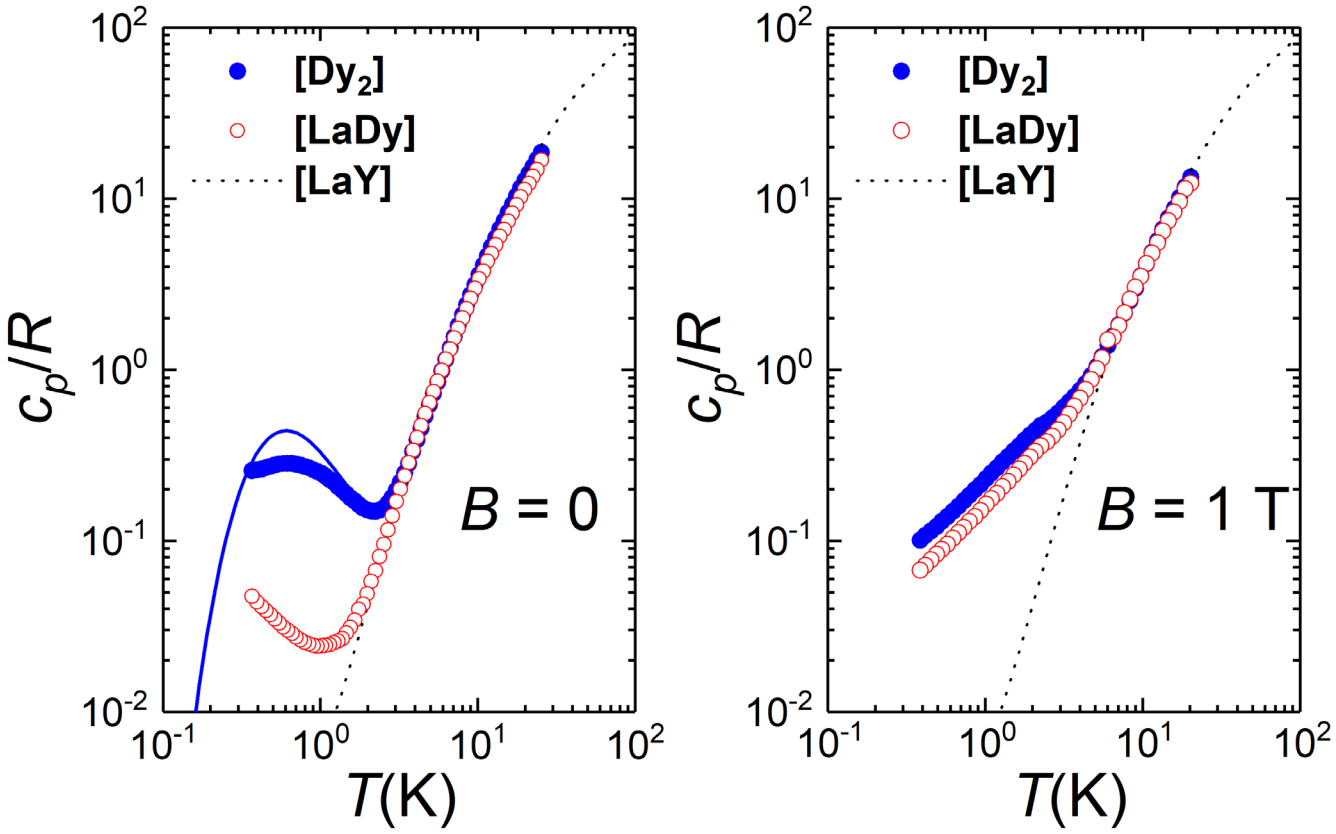


Figure S9. Comparison between the molar specific heat measured at zero magnetic field (left panel) and under a 1 T magnetic field (right panel) on bulk **[LaDy]** and **[Dy₂]** samples. Data measured on the diamagnetic **[LaY]** complex, which provides an estimation of the lattice contribution to $c_P/R$, are also shown as a dotted line. The solid line on the left hand side panel is a theoretical prediction based on the Hamiltonian (2) of the main text. The Schottky-like anomaly observed in the specific heat of **[Dy₂]**, and absent for **[DyLa]**, can be associated to the magnetic coupling between the two Dy(III) ions. The difference between $c_P$ of the two molecular complexes tends to vanish as the magnetic field dominates over the effect of intra-molecular spin-spin interactions.

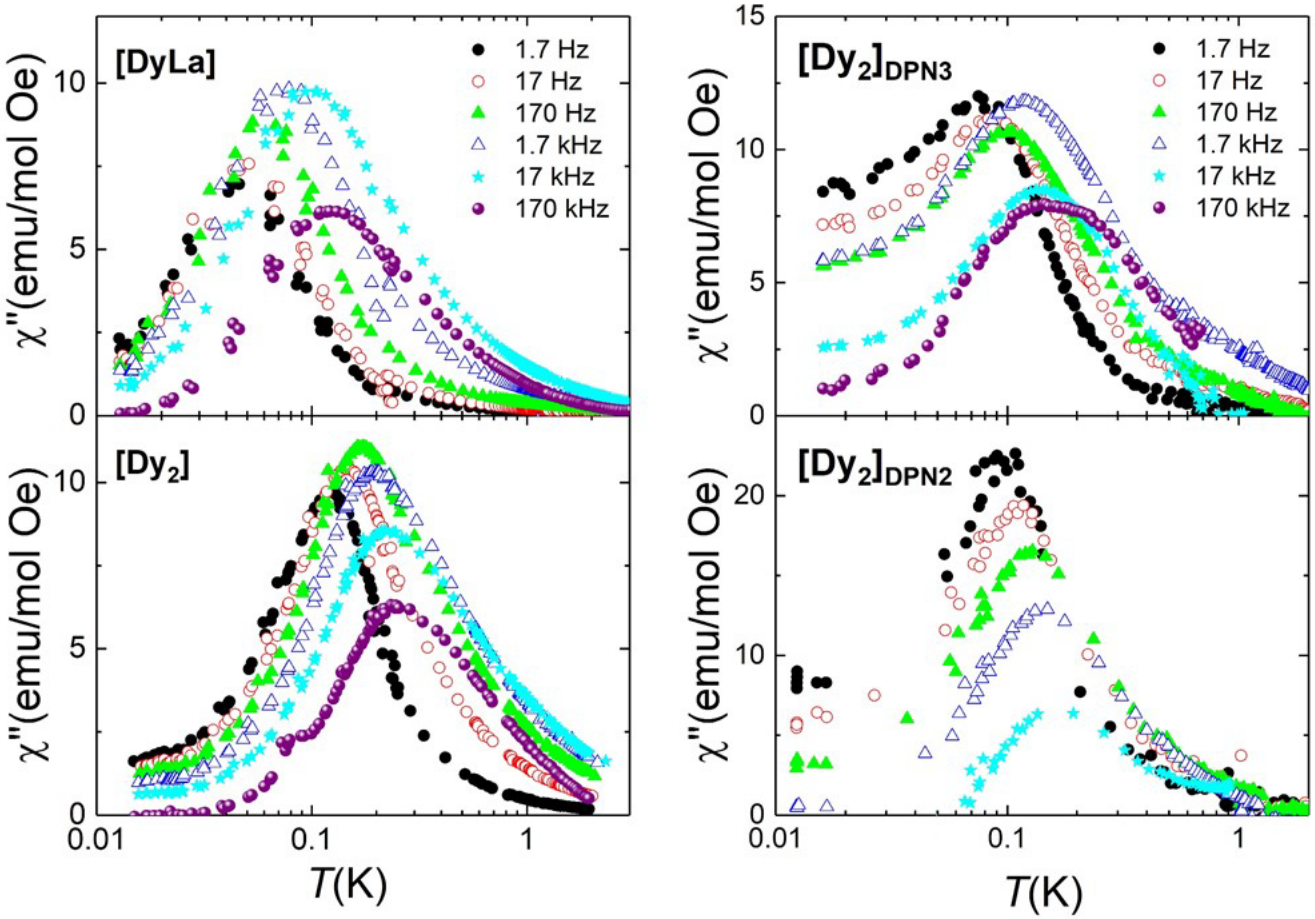


Figure S10. Imaginary component of the ac linear magnetic susceptibility of bulk **[LaDy]** and **[Dy$_2$]** (left), and of two **[Dy$_2$]** arrays deposited by DPN onto a micro-SQUID sensor (right) measured for different frequencies $\omega/2\pi$ of the excitation magnetic field. The maxima signal the condition $\omega\tau = 1$, with $\tau$ the characteristic spin relaxation time [1]. The data shown in Fig. 5 of the main text were obtained from these results. At any temperature, the relaxation time of all **[Dy$_2$]** samples is slower than that of **[LaDy]** (as evidenced by their $\chi$" maxima occurring at higher *T* for the same $\omega$), which shows that spin-spin interactions within each molecule hinder the spin reversal processes.

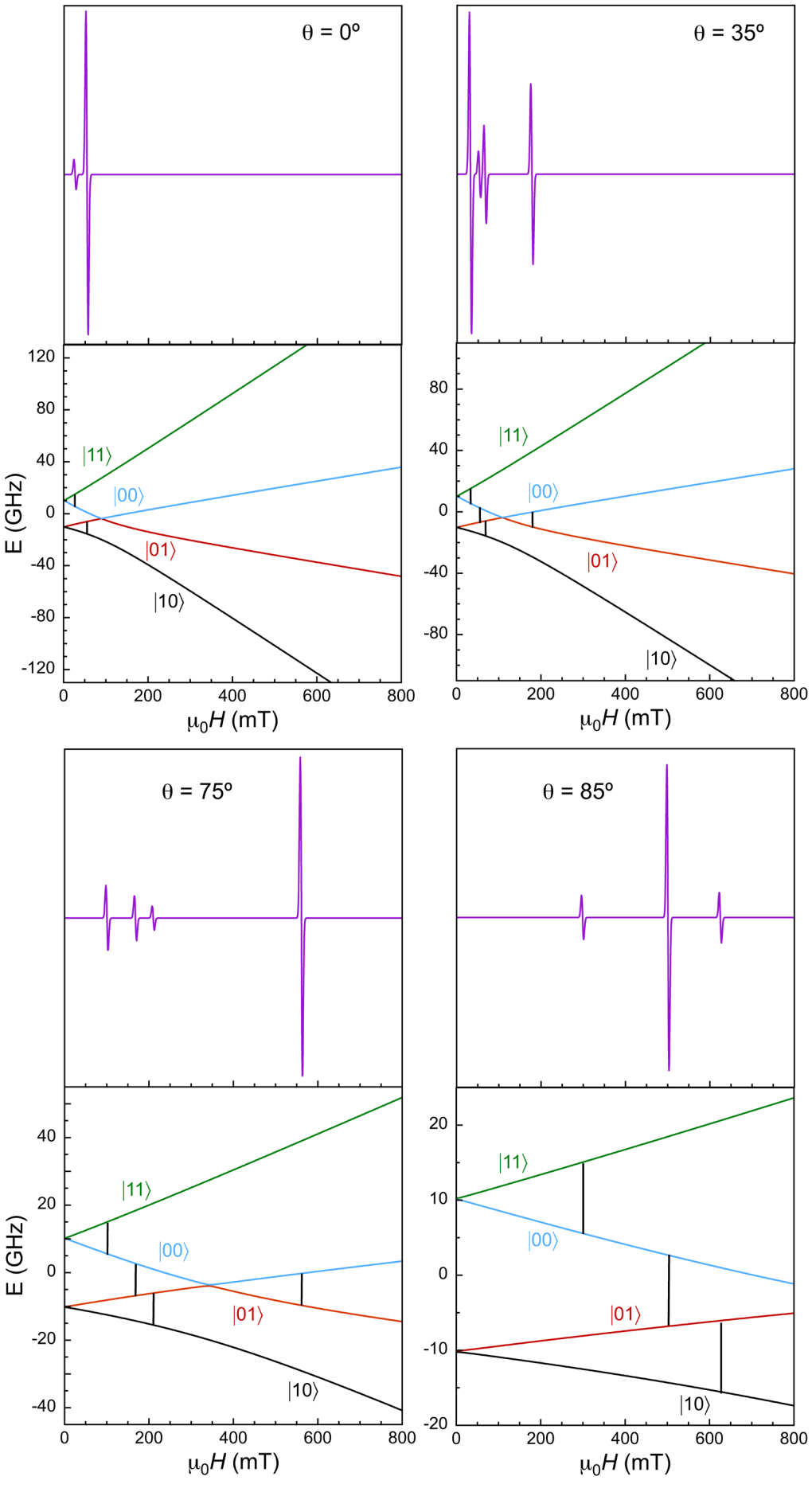
θ = 0°
θ = 35°
θ = 75°
θ = 85°
E (GHz)
μ0H (mT)
|11⟩
|00⟩
|01⟩
|10⟩

Figure S11. Simulated EPR spectra and energy levels schemes of an isolated **[$Dy_2$]** molecule for different magnetic field orientations as indicated. Simulations were done with Easyspin [2] using the same spin Hamiltonian parameters as for the bulk EPR spectrum and an hypothetic *P*1 single crystal, *i.e.* a unique **[$Dy_2$]** molecule. Theta is the angle between the z axis of the molecular frame, *i.e.* the anisotropy axis of $Dy_1$ site, and the magnetic field vector. Vertical bars indicate the expected transitions.

## 2. Ab-initio calculation of spin states and single-ion magnetic anisotropies in [LaDy] and [$Dy_2$]

### [LaDy]

The calculations confirm the high magnetic anisotropy of the Dy center in **[LaDy]**. The wavefunction of the ground state consists of almost pure $|M_J\rangle = |\pm 15/2\rangle$, well separated (118 $cm^{-1}$) from the first excited state (mainly $|M_J\rangle = |\pm 13/2\rangle$ but with some contributions of $|\pm 7/2\rangle$ and $|\pm 11/2\rangle$) (Table S4). Additionally, the ground state *g* tensor is found to be highly anisotropic ($g_x = 0.1$, $g_y = 0.1$, $g_z = 19.3$). The ground state magnetic anisotropy axis is shown in Figure S12.

Table S4. Computed energies levels (the ground state is set at zero), component values of the Lande factor *g* and wavefunction composition for each $M_J$ state of the ground-state multiplet for the Dy center in **[LaDy]**.

| | $E$ ($cm^{-1}$) | $g_x$ | $g_y$ | $g_z$ | WFT |
|---|---|---|---|---|---|
| 1 | 0.0 | 0.1 | 0.1 | 19.3 | $0.93\|\pm 15/2\rangle$ |
| 2 | 117.8 | 1.4 | 3.0 | 13.7 | $0.58\|\pm 13/2\rangle + 0.19\|\pm 7/2\rangle + 0.11\|\pm 11/2\rangle$ |
| 3 | 169.7 | 0.5 | 3.3 | 9.9 | $0.22\|\pm 9/2\rangle + 0.21\|\pm 5/2\rangle + 0.21\|\pm 11/2\rangle + 0.12\|\pm 3/2\rangle$ |
| 4 | 217.3 | 1.0 | 1.5 | 15.6 | $0.50\|\pm 11/2\rangle + 0.28\|\pm 13/2\rangle$ |
| 5 | 249.5 | 0.1 | 2.3 | 10.6 | $0.56\|\pm 9/2\rangle + 0.16\|\pm 7/2\rangle + 0.08\|\pm 11/2\rangle$ |
| 6 | 299.8 | 0.5 | 3.1 | 7.2 | $0.42\|\pm 7/2\rangle + 0.26\|\pm 5/2\rangle + 0.17\|\pm 1/2\rangle$ |
| 7 | 338.6 | 10.5 | 8.0 | 2.8 | $0.44\|\pm 3/2\rangle + 0.33\|\pm 5/2\rangle + 0.15\|\pm 1/2\rangle$ |
| 8 | 409.5 | 0.2 | 0.5 | 19.1 | $0.48\|\pm 1/2\rangle + 0.28\|\pm 3/2\rangle + 0.12\|\pm 5/2\rangle$ |

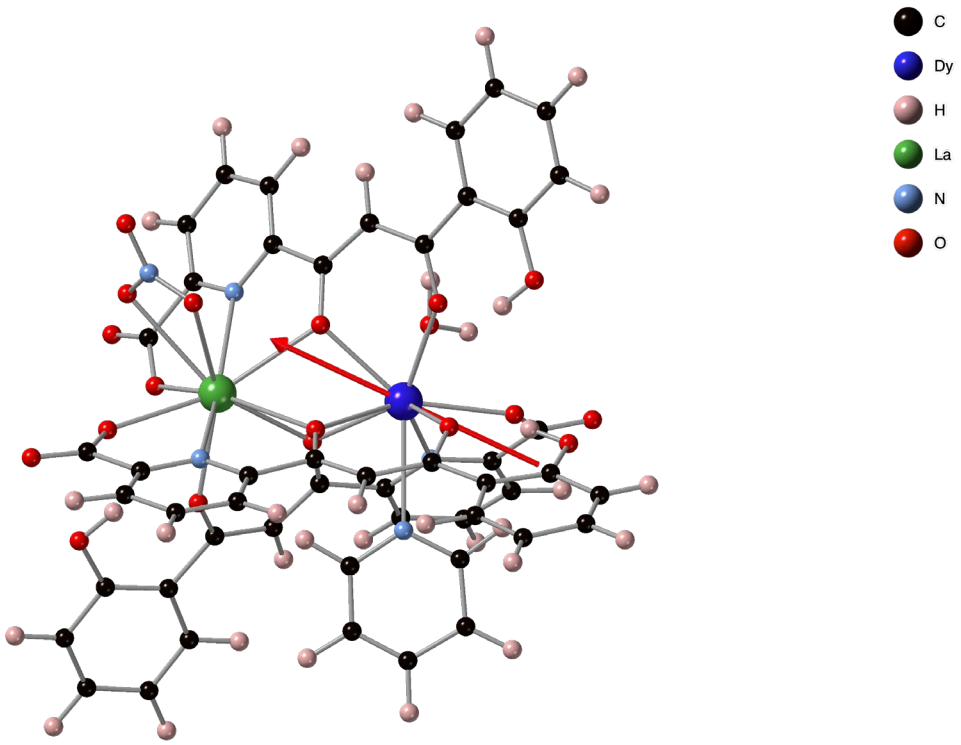


Figure S12. Anisotropy axis of the Dy(III) ion in **[LaDy]**.

**[$Dy_2$]**

For **[$Dy_2$]**, two separate calculations (replacing the second Dy(III) ion by a Y(III) ion) have been realized to get the magnetic properties of each Dy(III) center. In the calculations, $Dy_1$ corresponds to the Dy center bearing the Cl atom. The difference between both Dy ions is indeed clearly visible in the following tables. $Dy_2$ is much more Ising than $Dy_1$ with a *g* tensor close to what is expected for a pure $|M_J\rangle = |\pm 15/2\rangle$ ground-state ($g_x = g_y = 0$; $g_z = 19.4$). This is confirmed by the ground-state wavefunction that is also well separated (132 $cm^{-1}$) from the first excited state (mainly $|M_J\rangle = |\pm 13/2\rangle$) (Table S6).

The situation is markedly different for $Dy_1$ for which the ground-state anisotropy is much less axial (Table S5). The first excited state lies only 54 $cm^{-1}$ higher in energy. This explains the important mixing observed in the wavefunctions, and point to different static magnetic properties.

The magnetic axes are far to be collinear (Figure S13) with the axis on $Dy_2$ oriented in a similar way as in **[LaDy].** The angle $\delta = 72^{\circ}$ has been obtained from the scalar product of both axes. Their different orientations are explained by the electrostatic distributions around the Dy(III) ions that are different in both cases.

Table S5. Computed energies levels (the ground state is set at zero), component values of the Lande factor *g* and wavefunction composition for each $M_J$ state of the ground-state multiplet for $Dy_1$ center in **[$Dy_2$]**.

| | E ($cm^{-1}$) | $g_x$ | $g_y$ | $g_z$ | WFT |
|---|---|---|---|---|---|
| 1 | 0.00 | 0.1 | 0.3 | 18.2 | 0.66\|±15/2⟩ + 0.18\|±11/2⟩ + 0.13\|±13/2⟩ |
| 2 | 53.5 | 0.4 | 0.9 | 16.4 | 0.69\|±13/2⟩ + 0.13\|±15/2⟩ + 0.09\|±9/2⟩ |
| 3 | 91.9 | 0.1 | 1.6 | 17.0 | 0.25\|±1/2⟩ + 0.24\|±3/2⟩ + 0.19\|±5/2⟩ + 0.11\|±7/2⟩ |
| 4 | 137.8 | 2.2 | 4.1 | 11.7 | 0.43\|±11/2⟩ + 0.14\|±9/2⟩ + 0.13\|±15/2⟩ + 0.12\|±3/2⟩ + 0.12\|±1/2⟩ |
| 5 | 176.0 | 1.7 | 5.8 | 10.8 | 0.23\|±9/2⟩ + 0.21\|±1/2⟩ + 0.21\|±5/2⟩ + 0.13\|±3/2⟩ + 0.09\|±7/2⟩ |
| 6 | 223.1 | 2.4 | 4.1 | 10.1 | 0.36\|±7/2⟩ + 0.18\|±9/2⟩ + 0.15\|±1/2⟩ + 0.13\|±3/2⟩ + 0.09\|±5/2⟩ |
| 7 | 303.5 | 0.6 | 1.1 | 15.6 | 0.31\|±5/2⟩ + 0.20\|±7/2⟩ + 0.19\|±3/2⟩ + 0.14\|±9/2⟩ + 0.09\|±11/2⟩ |
| 8 | 435.8 | 0.1 | 0.1 | 19.3 | 0.21\|±1/2⟩ + 0.19\|±3/2⟩ + 0.17\|±7/2⟩ + 0.17\|±5/2⟩ + 0.16\|±9/2⟩ |

Table S6. Computed energies levels (the ground state is set at zero), component values of the Lande factor *g* and wavefunction composition for each $M_J$ state of the ground-state multiplet for $Dy_2$ center in **[$Dy_2$]**.

| | E ($cm^{-1}$) | $g_x$ | $g_y$ | $g_z$ | WFT |
|---|---|---|---|---|---|
| 1 | 0.00 | < 0.1 | < 0.1 | 19.4 | 0.93\|±15/2⟩ |
| 2 | 132.0 | 0.4 | 0.6 | 15.6 | 0.75\|±13/2⟩ + 0.11\|±7/2⟩ + 0.09\|±11/2⟩ |
| 3 | 206.4 | 1.5 | 2.1 | 11.0 | 0.34\|±11/2⟩ + 0.23\|±9/2⟩ + 0.15\|±5/2⟩ + 0.10\|±3/2⟩ + 0.10\|±7/2⟩ |
| 4 | 242.7 | 0.6 | 1.3 | 16.4 | 0.49\|±11/2⟩ + 0.20\|±13/2⟩ + 0.11\|±7/2⟩ |
| 5 | 291.0 | 0.0 | 1.8 | 10.6 | 0.63\|±9/2⟩ + 0.15\|±7/2⟩ |
| 6 | 355.2 | 6.5 | 5.5 | 3.2 | 0.44\|±7/2⟩ + 0.23\|±5/2⟩ + 0.13\|±1/2⟩ + 0.13\|±3/2⟩ |
| 7 | 416.1 | 2.6 | 3.6 | 12.0 | 0.42\|±5/2⟩ + 0.39\|±3/2⟩ + 0.10\|±1/2⟩ |
| 8 | 467.6 | 0.6 | 2.2 | 17.9 | 0.60\|±1/2⟩ + 0.30\|±3/2⟩ |

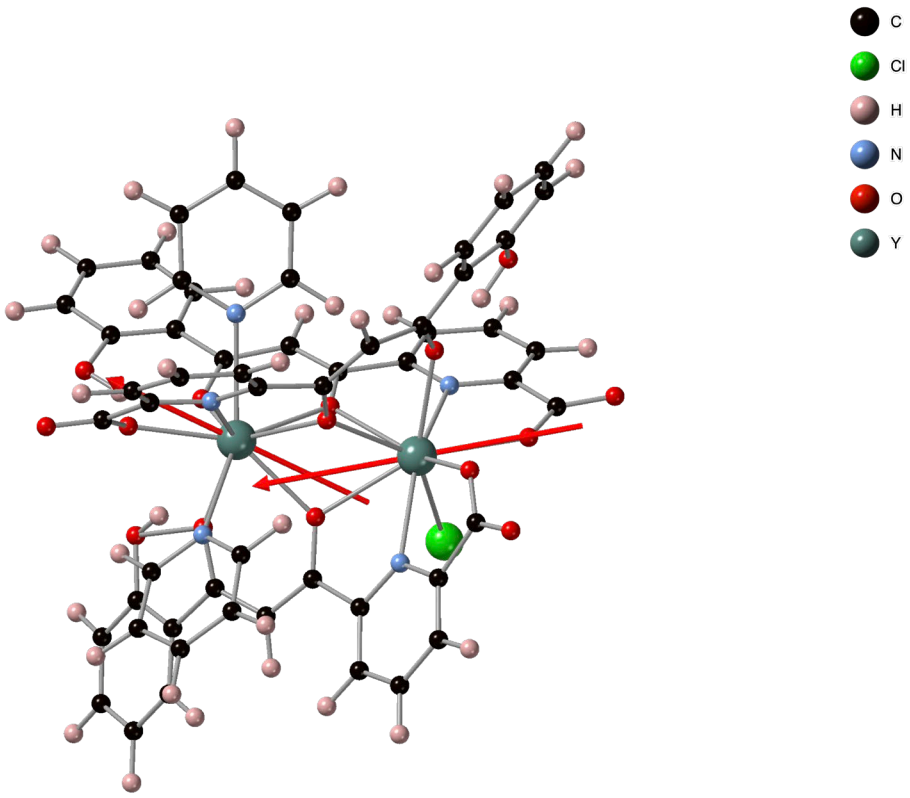


Figure S13. Anisotropy axes of the Dy(III) ions in **[Dy$_2$]**. The angle $\delta$ between the anisotropy axes of the two Dy ions $\overrightarrow{z_1}$ and $\overrightarrow{z_2}$ was obtained from the scalar product between the two corresponding vectors using the expression: $\delta = \cos^{-1}\left(\frac{\overrightarrow{z_1}\cdot\overrightarrow{z_2}}{\|z_1\|\|z_2\|}\right)$.

## 3. Numerical simulations of the magnetic flux generated by [$Dy_2$] arrays deposited onto micro-SQUID sensors.

Here we describe how to estimate the total flux that a given **[$Dy_2$]** molecular deposit, generates into the micro-SQUID pick-up coil. Assuming that each molecule can be approximated as point-like magnetic moment $\vec{\mu}$, induced by the excitation magnetic field, the flux it generates can be calculated as [3]:

$$\Phi = \frac{\vec{\mu} \cdot \vec{B}_{\mathrm{s}}}{i_{\mathrm{s}}}$$

Where $\vec{B}_{\mathrm{s}}$ is the magnetic flux created at the sample position by a current $i_{\mathrm{s}}$ circulating through the secondary coil. The induced magnetic moment, on the other hand, is determined by the linear magnetic susceptibility $\chi$ and by the magnetic field $\vec{H}_{\mathrm{p}}$ created by a current $i_{\mathrm{p}}$ circulating through the primary coil, resulting in $\vec{\mu} = \chi \vec{H}_{\mathrm{p}}$. The flux per unit of magnetic field is then given by:

$$\frac{\Phi}{H_{\mathrm{p}}} = \frac{i_{\mathrm{p}}}{B_{\mathrm{p}}} \frac{\chi}{i_{\mathrm{s}} i_{\mathrm{p}}} \vec{B}_{\mathrm{s}} \cdot \vec{B}_{\mathrm{p}}$$

Here, $\frac{B_{\mathrm{p}}}{i_{\mathrm{p}}}$.= $10^3$ G/A is the average magnetic flux created at the sample position by unit of current in the primary coil.

The molecules are distributed over the inner surface of the secondary coil. To calculate the total flux, we can divide the sample into $N_{\mathrm{cell}}$ cells and sum over the magnetic flux created by each cell $i$:

$$\frac{\Phi_{\mathrm{TOT}}}{H_{\mathrm{p}}} = \frac{i_{\mathrm{p}}}{B_{\mathrm{p}}} \frac{N_{\mathrm{mol}} \chi'_{\mathrm{mol}}}{i_{\mathrm{s}} i_{\mathrm{p}}} \frac{1}{N_{\mathrm{cell}}} \sum_{i}^{N_{\mathrm{cell}}} \vec{B}_{\mathrm{s},i} \cdot \vec{B}_{\mathrm{p},i}$$

Here, $N_{\mathrm{mol}}$ is the number of moles of sample and $\chi'_{\mathrm{mol}}$ is the molar susceptibility in cgs units, that we approximate by the simplest expression for a paramagnetic spin with a single relaxation time $\tau$

$$\chi'_{\mathrm{mol}} = \frac{\chi_T}{1 + (\omega\tau)^2}$$

where $\chi_T$ is the equilibrium susceptibility. In our calculations, we set it equal to the Curie-Weiss law that describes the response of bulk **[$Dy_2$]** (see Figs. 2 and S8, and Eq. (1) in the main text), i.e.

$$\chi_T = \frac{2N_A g_{\mathrm{eff}}^2 S(S+1)\mu_B^2}{k_B(T-\theta)}$$

with

$$g_{\mathrm{eff}} = 11.2;\ S = \frac{1}{2};\ \theta = -0.067\ K$$

For the relaxation time, we use the Arrhenius law

$$\tau = \tau_0 exp\left({}^{U}/_{k_B T}\right)$$

And the parameter *U* and $\tau_0$ found for each **[$Dy_2$]** sample (see Fig. 5 in the main text).

In order to determine $\Phi_{\mathrm{TOT}}$, the magnetic fields $\vec{B}_{\mathrm{s},i}$and $\vec{B}_{\mathrm{p},i}$ generated by the primary and secondary loops of the micro-SQUID susceptometer are estimated numerically using the 3D-MLSI software [4]. It allows calculating the magnetic flux created by the supercurrent distribution in a superconducting microcircuit with arbitrary shape. We use the actual dimensions of the primary and secondary coils as shown in Fig. S13a and the information on the sample geometry obtained from AFM experiments. The resulting position-dependent molar coupling is given in Fig. S14b in units of $\Phi_0$ mol/emu. The total flux can be then obtained as:

$$\frac{\Phi_{\mathrm{TOT}}}{H_p} = \chi_{\mathrm{mol}} \sum_{i}^{N_{\mathrm{cell}}} \text{Molar Coupling}_{\,i}$$

Notice that the 2D map in Fig. 3 of the main text shows the position dependent coupling in units of $\Phi_0$/emu. As can be seen in this figure as well as in panel b of Fig. S14, molecules located close to the pick-up coil contribute most to the net flux.

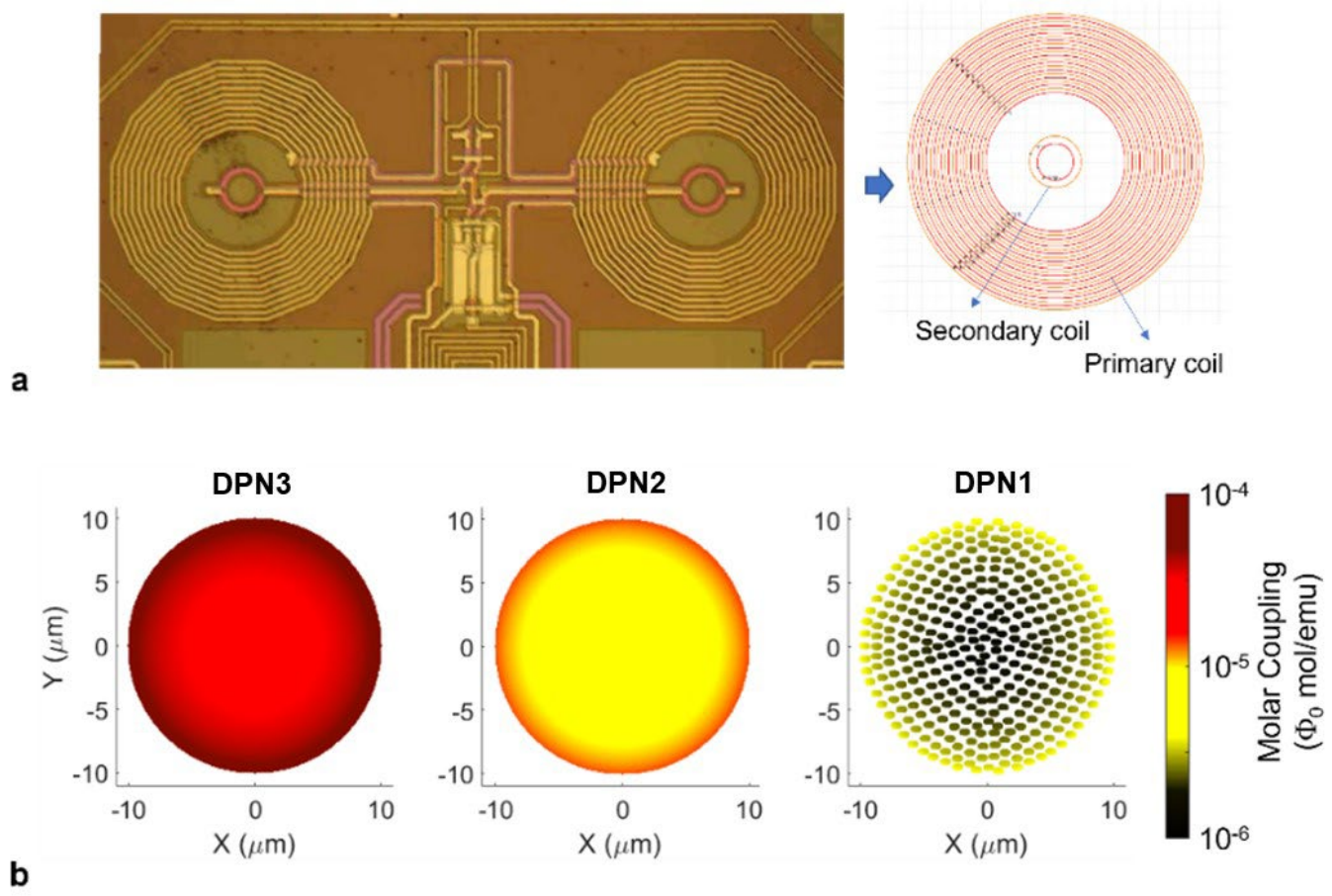


Figure S14: a) Left panel: optical image of the superconducting coils that form the micro-SQUID susceptometer. Right panel: circuit simulated with the 3D-MLSI software. b) Spatial distribution of the molar coupling for three **[$Dy_2$]** molecular deposits.

## 4. References

[1] K. S. Cole and R. H. Cole, *J. Chem. Phys.*, 1941, **9**, 341
[2] S. Stoll and A. Schweiger, *J. Magn. Reson.*, 2006, **178**, 42-55
[3] M. J. Martínez-Pérez, B. Müller, D. Schwebius, D. Korinski, R. Kleiner, J. Sesé, and D. Koelle, *Supercond. Sci. Technol.*, 2017, **30**, 024003
[4] M. M. Khapaev, M. Y. Kuprianov, E. Goldobin, and M. Siegel, *Supercond. Sci. Technol.*, 2002, **16**, 24